Università degli Studi della Calabria

Dottorato di Ricerca in Fisica

XIX CICLO (S.S.D. FIS/03)

Tesi di Dottorato

Diffusion and implantation of dopants in single-wall carbon nanotubes: a spectroscopic investigation of chemical and electronic properties

Claudia Giallombardo

Supervisore

Prof. Luigi Papagno

Coordinatore

Prof. Gennaro Chiarello

A. A. 2005-2006

"Non ci si deve mai sentire disarmati: la natura è immensa e complessa, ma non è impermeabile all'intelligenza"

Primo Levi

Contents

Introduction

The discovery of carbon nanotubes (CNTs), first observed in 1991 by Iijima [1] in the residual soot of fullerene synthesis, has opened a new era in material science, giving rise to the development of a wide research field. CNTs may consist of one (single-wall) or several (multi-wall) coaxial graphite layers rolled up in seamless cylindrical structures, with nanometre-size diameters. The nanotube electronic properties are affected by its structure, i.e., depending on the orientation of carbon atomic network with respect to the tube axis, they can be either metallic or semiconducting, with an energy gap inversely proportional to the diameter. The CNT electronic structure is characterized by sp^2 trigonal configuration of carbon atoms, which form σ bonds lying on the tube walls, and π bonds perpendicular to the tube axis. The strong covalent interaction occurring between σ orbitals accounts for CNT unique tensile strength and elastic modulus along the axial direction. The remarkable mechanical, chemical, transport and field emission properties make CNTs promising materials for several applications, including flat-panel displays, probes for scanning microscopes, electrode materials for batteries, energy storage

systems, chemical sensors, and nanoscale electronic devices. Moreover, because of their high aspect ratio, CNTs can be regarded as one-dimensional systems, which constitute at present time a fundamental topic in solid state physics. Commercial applications and experimental characterization require the availability of large quantities of purified CNTs, therefore many efforts are devoted to improve the efficiency of synthesis and purification methods, through which arrangements of both aligned or randomly oriented tubes can be obtained. The formation of bundles containing several SWCNTs with slightly different diameter and chirality usually occurs during growth processes, and further procedures must be carried out to obtain isolated tubes. As regards electronic behavior, it is well known that samples consist of a mixture of metallic and semiconducting tubes, and it is still not possible to select them in order to achieve homogeneous systems.

Several experimental techniques have been employed to probe the physical properties of individual tubes as well as disordered CNT bundles. Moreover, the occurrence of large empty spaces between tubes in a bundle has suggested the possibility of realising, in analogy with graphite and fullerenes, intercalation compounds. CNT electronic properties can indeed be engineered through proper doping procedures with electron donors or acceptors [2], achieved through the introduction of atomic and molecular species; among donor atoms, alkali metals and nitrogen attract particular interest. It is well known that alkali doping remarkably modifies several CNT electronic and transport properties, while nitrogen atoms have suitable dimension to achieve substitutional n-doping, which may be exploited to improve CNT field-emission properties [3].

This thesis concerns an investigation of chemical and electronic properties of sodium-, lithium- and nitrogen-doped SWCNT bundles, performed by Electron Energy Loss Spectroscopy and Photoemission Spectroscopy. As for the alkali doping, recent photoemission studies on potassium- and lithium-intercalated single-wall carbon nanotube bundles [4,5] have revealed the occurrence of an alkali-induced transition from a one- toward a three-dimensional system. It has been

suggested that K-doping produces the metallization of semiconducting tubes, therefore making homogeneous the electronic structure of the sample, while Li atoms give rise to cross-links among tubes; both these mechanisms can indeed account for the detected alteration of the CNT's one-dimensional nature. We have compared of the effects induced by sodium and lithium intercalation on valence band and core level states, in order to get a better insight into the nature of the interaction involving different alkali species and the nanotube network. Our results have pointed out that lithium atoms seem to form covalent-like bonds with nanotubes, leading to evident modifications of the electronic properties, while sodium has a ionic interaction with the system and causes only a Fermi level shift due to the charge transfer, without affecting the electronic band structure.

As regards N-doping, several methods, like arc-discharge and pyrolysis have been employed to incorporate nitrogen atoms into CNTs [6]. However, it has been shown that significant amounts of nitrogen impurities do not occupy the expected substitutional sites, as they undergo chemisorption or bind to irregular sp^3 structures of the nanotube network. Some theoretical studies have suggested that better performances could be achieved through the ion implantation technique [7]. So, we have carried out high-energy N_2^+ ion irradiation on SWCNT bundles to probe the real effectiveness of this technique. Our results have shown that nitrogen atoms bind to CNTs in three different configurations; the substitutional impurities are stable also after high-temperature annealing and induce an enhancement of the density of states near the Fermi level.

The thesis is organized as follows. Chapter 1 and 2 contain a brief description of CNTs structural and electronic properties, and a general survey of the state of the art concerning doped CNTs, respectively. A description of the experimental apparatus and techniques employed in our measurements can be found in chapter 3. In chapter 4 and 5 the experimental results on alkali and nitrogen doping of SWCNT bundles are presented and discussed. Finally, in chapter 6 some remarkable results are introduced which relate to the structural

characterization of multi-wall carbon nanotubes (MWCNTs), synthesized by arc-discharge method in helium atmosphere. Raman measurements have revealed indeed the occurrence of carbon linear chains encapsulated in the innermost tube and lying along its axis; the recent discovery of carbon linear chains inserted into multi-wall CNTs [8] has evidenced that nanotubes constitute a suitable environment for very long and stable linear arrangements of sp-hybridized carbon atoms. Since isolated chains are rather known to be energetically unstable, these findings pave the way for further progress in the realization of carbon nanowires, which might have several technological applications. Furthermore, a Raman temperature-dependent study has allowed us to observe for the first time the occurrence of a reversible phenomenon involving the chains, which might be representative of temperature-driven modifications of carbon atom bond distances.

Chapter 1

Carbon nanotubes

1.1 Structure of carbon nanotubes

Carbon atoms can arrange themselves in several aggregation forms, with C-C chemical bonds characterized by different types of hybridization of the valence atomic orbitals $2s^2\ 2p^2$. Carbon hybridized states are sp^2 and sp^3 in graphite and diamond respectively, the first having planar trigonal structure and the second three-dimensional tetragonal structure. In 1985 Kroto et al. [9] discovered fullerenes, soccer ball-like molecules in which the pure carbon atoms are bonded in hexagon and pentagon configurations; pentagons are distributed in order to obtain the required curvature for closing the structure. As for the electronic properties, fullerenes exhibit a semiconducting behavior, while graphite is a semimetal and diamond is an insulator.

In 1991 Iijima [1] observed for the first time multi-walled carbon nanotubes (MWCNTs) on the surface of carbon electrodes used for the synthesis of fullerenes, and two years later he also discovered single-walled carbon nanotubes (SWCNTs) [10]. The structure of a SWCNT can be visualized as one graphite sheet rolled up to form a cylinder with a diameter of about 1-2 nm; MWCNTs consist instead of

several coaxial cylinders and have diameters ranging from 10 to 30 nm. The distance between adjacent walls is about 3.4 Å, nearly equal to the interlayer distance in graphite. Carbon nanotubes length can be up to hundred microns; since the order of magnitude of the ratio between length and diameter is 10^4-10^5 they can be considered as quasi-one-dimensional nanostructures. The ends of tubes are closed by caps consisting of hemispherical fullerenes, with a particular distribution of hexagons and pentagons such that the caps fit perfectly the tube.

The real lattice structure of a single layer of graphite (*graphene*) results from a Bravais lattice ($\boldsymbol{a}_1$, $\boldsymbol{a}_2$ primitive vectors) with a two-atom basis, and is named honeycomb lattice due to the hexagonal arrangement of carbon atoms. In the reciprocal lattice ($\boldsymbol{b}_1$, $\boldsymbol{b}_2$ primitive vectors) the high symmetry points Γ, K, and M correspond, respectively, to the center, the corner and the half side of the hexagonal first Brillouin zone (shaded area in fig. 1.1(b)). A nanotube is identified by the chiral vector, defined as

$$\boldsymbol{C}_h = n\boldsymbol{a}_1 + m\boldsymbol{a}_2 \tag{1.1}$$

where n, m are integers [11]. A SWCNT can be obtained wrapping the graphene sheet so that the ends of the chiral vector (O and A in fig. 1.1(c)) coincide.

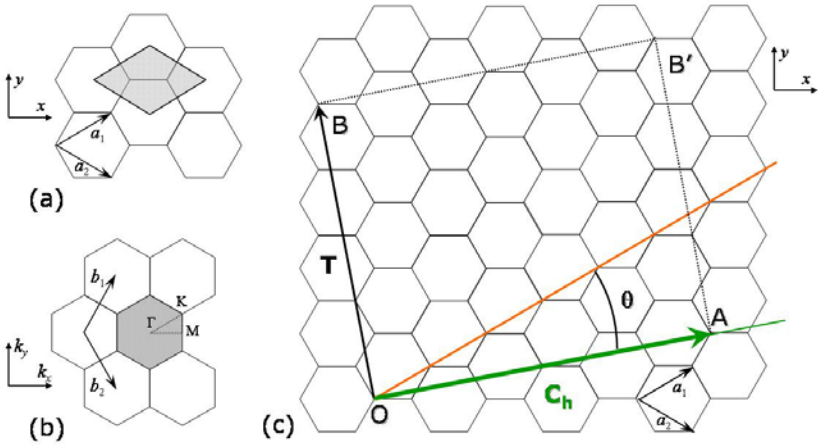

Fig. 1.1 – (a) Real and (b) reciprocal lattice of graphene. (c) Chiral ($\mathbf{C}_h$) and translational ($\mathbf{T}$) vectors of carbon nanotubes

The chiral vector and the translational vector $\mathbf{T} = t_1\boldsymbol{a_1} + t_2\boldsymbol{a_2}$ (t_1, t_2 integer), that is parallel to the tube axis, define the unit cell of the nanotube, while the chiral angle θ ($0 \le \theta \le 30°$) between the chiral vector and $\boldsymbol{a}_1$ describes the orientation of the hexagons of the honeycomb lattice with respect to the tube axis.

The direction of the chiral vector is perpendicular to the tube axis, while its modulus is the length of the circumference, so the diameter of the tube is

$$d = \frac{|\boldsymbol{C}_h|}{\pi} = \frac{\boldsymbol{a}}{\pi}\sqrt{n^2 + m^2 + nm} \tag{1.2}$$

in which $\boldsymbol{a}$ is related to the nearest-neighbor distance between carbon atoms through $\boldsymbol{a} = \sqrt{3}\boldsymbol{a}_{C-C} = 2.46$ Å.

If $n = m$ nanotubes are called *armchair* ($\theta = 30°$), if $m = 0$ they are called *zigzag* ($\theta = 0°$); these two names describe the atomic configuration along the circumference (see fig. Y). All the other (n,m) tubes, with $n \neq m$, are called *chiral*.

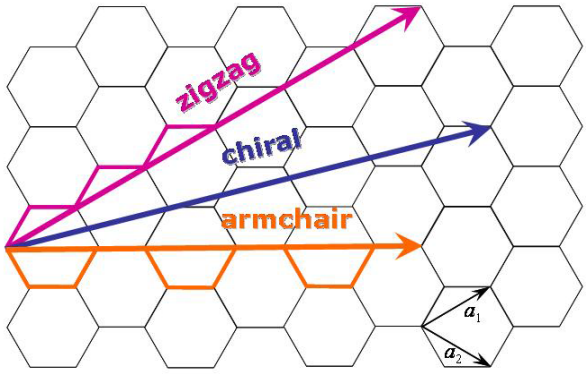

Fig. 1.2 – An example of chiral vectors corresponding to zigzag, chiral and armchair nanotubes

The structure of CNTs can be investigated by High-Resolution Transmission Electron Microscopy (HRTEM), which allows the identification of tubes and structural defects, and the determination of diameters distribution. Moreover, atomic resolution can be achieved with Scanning Tunneling Microscopy (STM) images, from which it is possible to establish also the tube diameter and chirality.

1.2 Band structure of graphene and SWCNTs

According to the zone folding method, the electronic structure of CNTs can be obtained from that of graphene, taking into account boundary conditions arising from the rolling of the graphene sheet. In graphene, the carbon 2s, $2p_x$ and $2p_y$ atomic orbitals hybridize in a planar sp^2 configuration and give rise to σ planar bonds, while the $2p_z$ wave functions form the π bonds perpendicular to the plane.

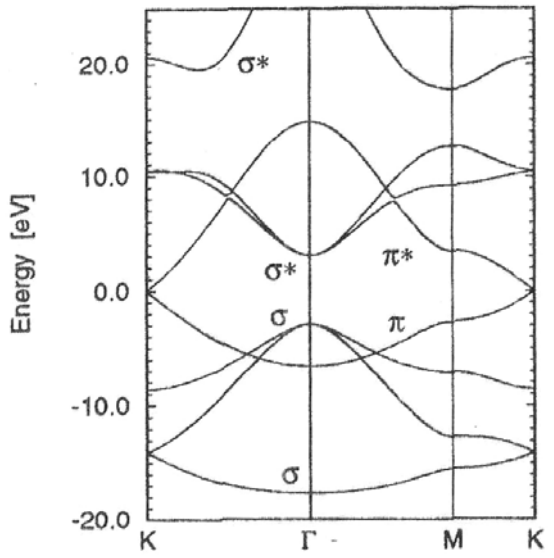

Fig. 1.3 – Band structure of graphene [11]

Since the unit cell includes two atoms, there are two π bands and six σ bands: fig. 1.3 shows the energy dispersion relations of each band along the high symmetry directions, obtained with a 2D tight-binding calculation [11]. At T=0K the π bonding band is completely filled and the π^* anti-bonding band is empty; moreover, the π and π^* bands are degenerate at the six K points, which are placed at the corners of the first Brillouin zone. Since the Fermi level coincides with the energy of the crossing, and the density of states at the Fermi level is zero, graphene is a zero-gap semiconductor. Three-dimensional graphite is instead a metal, because the interactions among layers cause an overlapping of the bands, which are partially filled at T=0K. We can notice from fig. 1.3 that, around the K point, the dispersion

of π bands is approximately linear next to the Fermi level. In the following discussion about CNT electronic properties, we will focus on the states deriving from π valence and conduction bands, which cross at the Fermi level and give the main contribution to the band structure close to the Fermi energy (σ states are instead much far from E_F, as the smallest gap between σ and σ^* band is about 11 eV at the Γ point).

Since a nanotube can be regarded as infinitely long, the reciprocal wave vector $\boldsymbol{K_2}$ corresponding to the translational vector **T** is continuous, while a quantization of the wave vector $\boldsymbol{K_1}$ in the direction of $\boldsymbol{C_h}$ occurs, according to the boundary condition $\boldsymbol{C_h} \cdot \boldsymbol{k} = 2\pi l$ (l integer). If N is the number of hexagons contained in the CNT unit cell, there are N allowed values of k in the circumferential direction, which can be represented in **k** space by N lines parallel to the axis direction. The number of lines and their orientation with respect to the unit cell depend both on tube chirality and diameter. According to the zone-folding approximation, the electronic states of a nanotube are given by the graphene band structure cut along the allowed k lines (see fig. 1.4(b)).

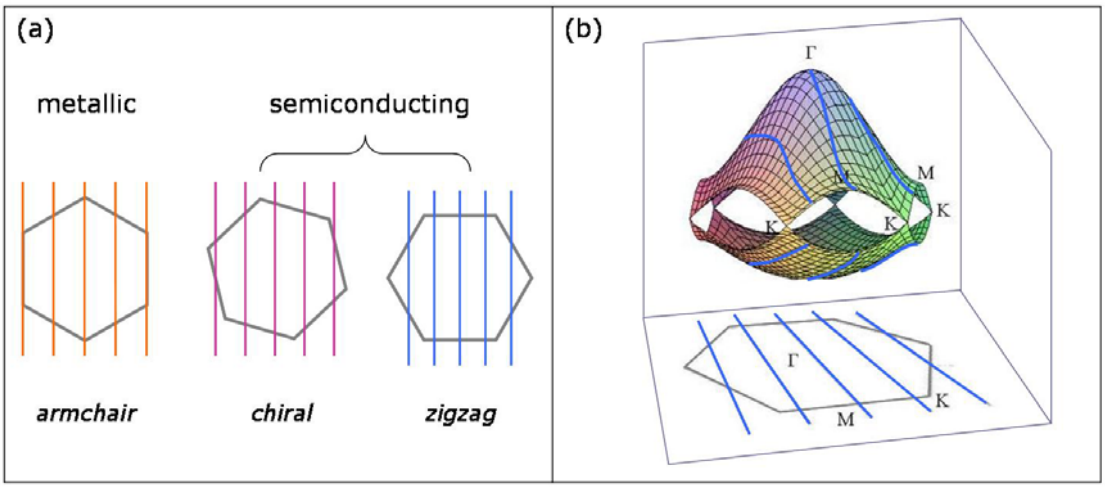

Fig. 1.4 – (a) The first Brillouin zone of graphene (hexagons) and the allowed electronic states of nanotubes (lines). If lines cross K points they are metallic, otherwise they are semiconducting. In panel (b) an example of the cuts of the π and π^* bands of graphene, from which that of nanotubes can be inferred, is represented.

Energy dispersion plots of CNTs (fig. 1.5) are made of N pairs of one-dimensional dispersion relations versus the wave vector in the direction of $\boldsymbol{K_2}$, obtained by cutting the two-dimensional graphene band structure. The two π and π* bands corresponding to an allowed value of $\boldsymbol{K_1}$ are separated by an energy gap, unless a discretization line crosses a K point of the graphene first Brillouin zone. In this case the nanotube is metallic, as it has two bands crossing the Fermi level; it has been proved [12] that this happens if n-m is a multiple of 3, otherwise the (n,m) tube is semiconducting with a finite band-gap. It follows that approximately one third of CNTs are metallic and two thirds are semiconducting; armchair (n,n) CNTs are always metallic, while zigzag (n,0) tubes are metallic if n is a multiple of 3. Moreover, the energy gap of semiconducting tubes increases with decreasing diameters according to the relation

$$E_g = \frac{2\gamma_0 a_{C-C}}{d} \tag{1.3}$$

where $\gamma_0 = 2.5\,\text{eV}$ and $a_{C-C} = 1.42\,\text{Å}$ are the graphite overlap integral and the nearest-neighbor C-C distance on a graphene sheet, respectively.

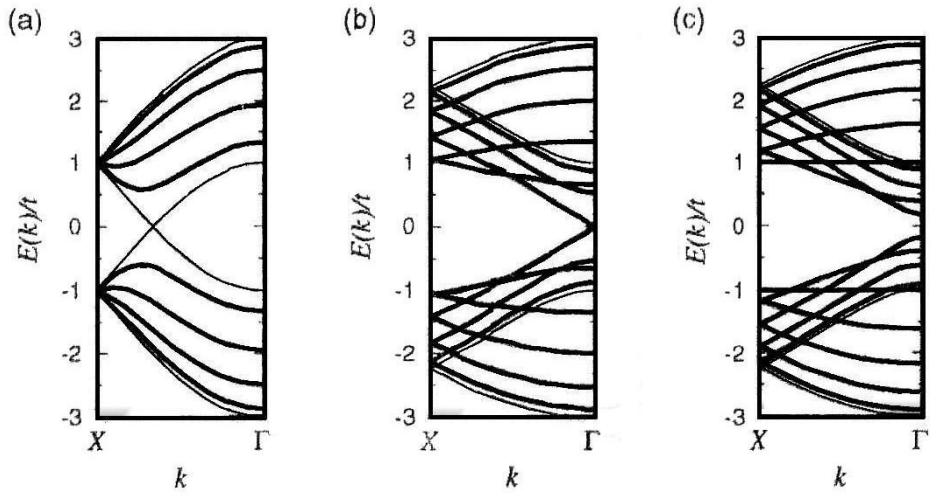

Fig. 1.5 – Energy dispersion relations for (a) armchair, (b)-(c) zigzag nanotubes [11]; X points correspond to k = ± π/a and to k = ± π/a√3 for armchair and zigzag tubes, respectively

It is worth noting that the zone-folding approximation gives reliable results for states close to the Fermi level and for tube diameters larger than 1.5 nm. For very small tubes, in fact, it is necessary to take into account also curvature effects, which lead to band structure modifications induced by the hybridization of π^* and σ^* orbitals [13].

1.3 Density of states

The density of electronic states (DOS - $n(E)$) of a system is strictly connected to its dimensionality. It is well known [13] that, for parabolic band dispersion, $n(E) \propto \sqrt{E}$ in three-dimensional systems, while $n(E)$ is a step-like function in two-dimensional solids and $n(E) \propto 1/\sqrt{E}$ for one-dimensional systems (fig. 1.6).

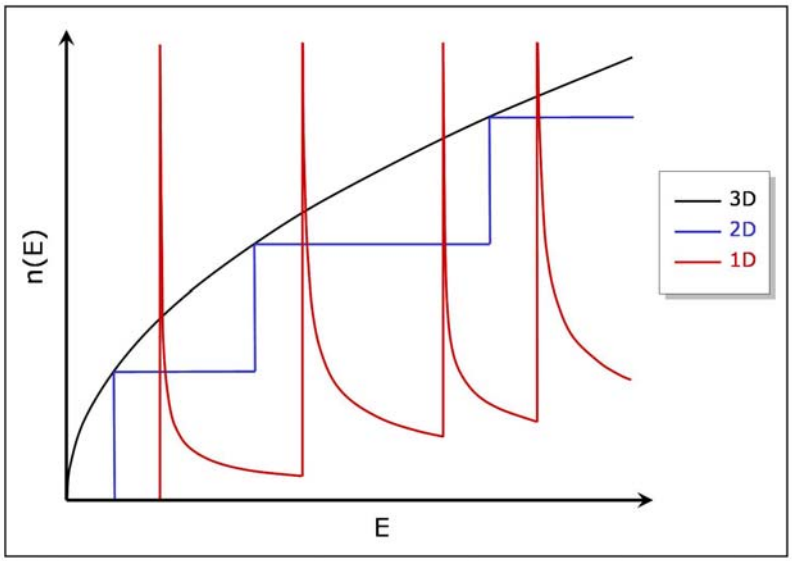

Fig. 1.6 – DOS behavior for 3D-, 2D- and 1D-systems

In CNTs, as all one dimensional systems, the DOS is proportional to $\left|\frac{dE(k)}{dk}\right|^{-1}$, where $E(k)$ is the band dispersion relation [14]. Hence, the DOS is characterized by a series of divergences, called *van Hove singularities* (vHs), occurring at energies such

that $\frac{dE}{dk}=0$. These states strongly affect several physical properties, as they are associated to an extremely high DOS.

Because of linear dispersion of the π bands crossing at E_F, the DOS of metallic CNTs is constant around the Fermi level (fig. 1.7(a)), and the width of the plateau is roughly three times as large as the band gap of a semiconducting tube having the same diameter [15]. Moreover, for semiconducting tubes, the DOS is zero in an energy range centered around the Fermi level and corresponding to the gap, which is approximately equal to the distance between the first couple of vHs (fig. 1.7(b)).

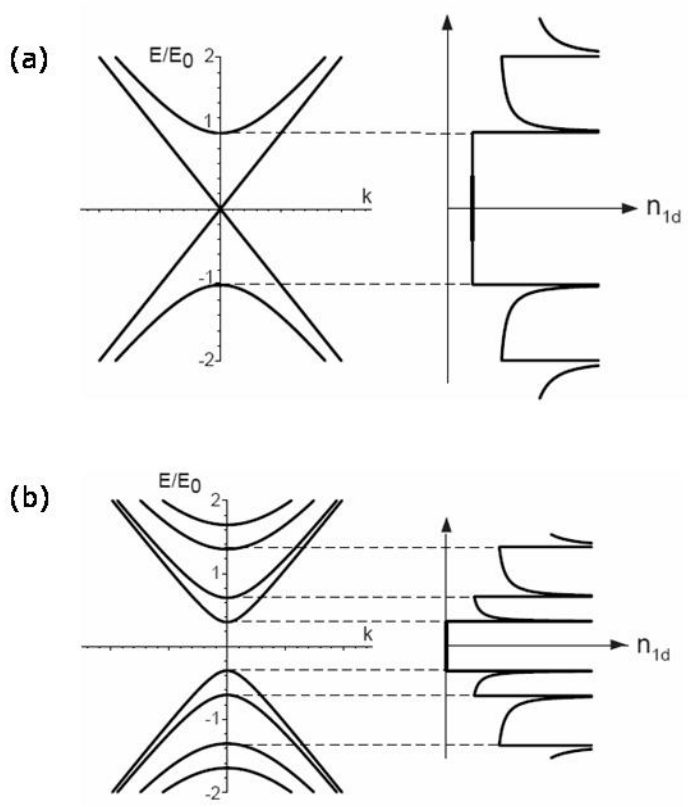

Fig. 1.7 – Energy dispersion relations and corresponding density of states of (a) metallic and (b) semiconducting CNTs

The theoretical results [14] about the DOS behavior for CNTs have been verified through Scanning Tunneling Spectroscopy (STS) [16-18], Raman scattering [19] and optical absorption measurements [20]. STS results [16,17] have provided the first evidences that CNT electronic properties depend on both tube diameter and chirality. Moreover, vHs and band gaps values consisting with the theoretical predictions have been observed. In STS experiments, an STM tip is placed over the sample, and the tunneling current is recorded as a function of the voltage between the sample and the tip; the spectra of normalized differential conductance $(dI/dV)/(I/V)$ vs. voltage give a measure of the electronic DOS. This technique has the further advantage that a simultaneous structural analysis can be carried out acquiring STM images. STS investigations have also pointed out that only armchair tubes are truly metallic and the small energy gaps (about 50-100 meV) occur in metallic zigzag CNTs [21]; these gaps depend inversely on the square of the tube radius and arise from the finite curvature effects mentioned in the previous paragraph.

It is well known that growth techniques usually produce SWCNTs packed in bundles (or ropes) containing 20-100 tubes, with a random distribution of diameters and chiralities, held together by van der Waals forces and arranged in a two-dimensional triangular lattice structure. Tight binding calculations [22] have showed that pristine SWCNT bundles are as well representative of one-dimensional systems because of the weak interaction among tubes. The occurrence of vHs in SWCNT bundles has been confirmed both by angle-integrated photoemission [23] measurements and an STS study [21], which has showed also that pseudo-gaps of approximately 100 meV occur in bundles consisting only of armchair tubes. Since in this case the DOS at the Fermi level is strongly reduced but not suppressed, this is not a curvature effect, but rather a consequence of a break of symmetry resulting from the intertube interactions. Hence, in bundles the electronic band structure next to the Fermi level suffers some changes, while the location of vHs is quite the same with respect to isolated tubes.

Chapter 2

Doped carbon nanotubes

A great deal of experimental and theoretical studies concern the effects induced on CNTs by suitable doping with donor or acceptor species. Transport, optical and electronic properties of CNTs can be modified through several procedures, such as intercalation, chemical functionalization, electrochemical and substitutional doping. The attainment of extensive knowledge in this field is very important as the ability of tailoring CNT properties may contribute to the fulfilment of innovative electronic nano-devices.

2.1 Alkali-metal intercalation

The similar structure of graphite and nanotubes has suggested to try controlling CNT properties through the insertion of alkali atoms, which accomplishes n-type doping, adopting the same method used for Graphite Intercalation Compounds (GICs) [24,25]. Alkali-doped SWCNT ropes and mats exhibit both an increase of electronic conductivity, and a shift of high-frequency tangential Raman active modes toward lower frequencies [26-28]. Moreover, UPS

measurements carried out on Cs-doped SWCNT bundles reveal a remarkable decrease of the work function (about 2.4 eV) upon Cs intercalation [29], and the alkali-induced reduction of work function has been confirmed by first-principles calculations [30]. All such results provide evidence for an increase of charge carriers concentration due to electron transfer between the adsorbed element and SWCNTs. TEM and EELS measurements [31] have showed that alkali-metal deposition introduces structural disorder in the bundles and that de-intercalation is achieved after exposing the sample to air. An extensive EELS study on the effects induced by Na, K, Rb, Cs on SWCNT mats [32] has showed that these alkali do not hybridize with carbon atoms and that an increase of the intertube distance in bundles occurs for increasing dopant size.

Alkali metal adsorption takes place in the interstitial bundle sites; Li atoms, due to their small radius, can also enter inside the hollow tubes, and hence higher lithium intercalation density can be achieved in CNTs than in graphite [33]. For this reason, Li-intercalated nanotubes are considered promising materials for improving performances of both anode materials in rechargeable batteries, and energy storage devices. First experiments performed on alkali-doped SWCNTs at ambient pressure and moderate temperatures had showed an enhanced hydrogen storage capability [34]. This effect was attributed to dissociative adsorption induced by alkali metals, in contrast to non-dissociative physisorption occurring on pristine samples [35,36], but further experiments pointed out that moisture was responsible of most of the hydrogen uptake [37,38]. First-principle calculation results have indicated that H-dissociative adsorption can occur on defects but not on Li-doped SWCNTs, because energy barriers are only slightly reduced by Li charge transfer [39], and a lack of significant hydrogen storage capability of purified SWCNTs has been proved by recent TEM analysis [40]. It seems, therefore, that at room temperature an alkali-induced hydrogen uptake does not really take place [41], while defect sites induce an increase of H adsorption in pristine as well as in alkali-doped samples.

Some experimental studies have established that the maximum Li intercalation density, which is LiC_6 for both closed-end nanotubes and graphite, can be doubled upon chemical etching [42]. This effect is likely due to an increased number of available adsorption sites, since in the etched tubes open ends and sidewall defects make it possible diffusion inside the tubes, in addition to the usual channels of bundle interspaces. According to theoretical calculations, Li atoms distribute on the tube walls and on high-symmetry sites in order to maximize the Li-Li distance, so that the electrostatic repulsion is reduced; moreover, both inner and outer adsorption sites are stable up to the intercalation limit [43,44]. As for electronic properties, an almost complete charge transfer from lithium to the tubes has been predicted, and the formation of new states in the conduction band has been found, while valence band states are quite unperturbed [43].

Since transport measurements have pointed out that individual metallic SWCNTs behave as quantum wires [45], several studies on alkali-doped CNTs concern the topic of one-dimensional system properties. It is well known that the strong correlation effects occurring in one-dimensional metals cause the failure of the Fermi Liquid theory. These systems can rather be described by the Tomonaga-Luttinger-Liquid (TLL) model: Luttinger liquids present many fascinating properties, among which spin-charge separation and ballistic electronic transport are worth a mention [13]. A TLL is characterized by the g parameter, which accounts for the strength of interaction between electrons, and takes values much smaller than 1 if electron repulsion is strong, whereas $g = 1$ for non-interacting electron gas. Some theoretical studies have established that a SWCNT can be regarded as a one-dimensional system along the axis direction and that the value of Luttinger parameter should be $g < 1$, due to long-range Coulomb interaction between electrons [46,47]. Moreover, transport properties measurements have evidenced the existence of strong electron correlations [48], yielding a Luttinger parameter $g = 0.28$ [45,49] for SWCNT tubes or ropes with finite length. The tunneling

amplitude of an electron in a Fermi liquid is predicted to be energy-independent, while for Luttinger liquids is expected to follow an anomalous power law dependence on the energy of tunneling electrons. This behavior leads to a power law scaling of low-bias conductance ($G \propto T^{\alpha}$) and high-bias differential conductance ($dI/dV \propto V^{\alpha}$) with respect to temperature and bias voltage, respectively. The parameter α depends on the size of the Coulomb interaction and can be expressed as $\alpha_{bulk} = (g^{-1} + g - 2)/8$ or $\alpha_{end} = (g^{-1} - 1)/4$, depending on whether tunneling occurs into the side or into the end of the TLL. Theoretical calculations have showed that for SWCNTs $g \approx 0.2$, $\alpha_{bulk} \approx 0.4$, and $\alpha_{end} \approx 1$ [47]. Conductance measurements performed on SWCNT ropes have proved the power-law dependence of G on temperature, leading to experimental values of the exponent α in good agreement with the theoretical predictions [50]. Moreover, in TLL liquids the spectral function is predicted to have a power-law dependence $n(E_B) \propto |E_B|^{\alpha}$ on the binding energy near the Fermi level. A recent angle-integrated photoemission study [23] on SWCNT bundles has provided a confirmation of TLL behavior in CNTs. According to this investigation, the low-energy valence band profile, which is a direct measure of the DOS near E_F, follows at low temperatures a power-law scaling with exponent $\alpha = 0.46$, leading to a Luttinger parameter $g = 0.18$. High-resolution photoemission measurements, carried out at T=70K with a Scienta SES 300 analyzer, have allowed us to observe the same profile on our commercial SWCNT bucky-paper (employed in all the experiments described in chapters 4 and 5). The value of α, obtained via a linear fit of the double-logarithmic representation of the low-energy valence band spectrum (see inset in fig. 2.1), is 0.43, which is in good agreement with the results reported in the literature.

We must take into account that the interaction within a bundle may induce the opening of a small gap, so all the tubes would be narrow gap semiconductors and could not be described by the Luttinger model. However, Maarouf et al. have deduced, from tight binding calculations on nanotube ropes [22], that a pseudo-gap

of about 0.1 eV is observed for a bundle consisting of only (10,10) metallic tubes, while in a bundle of tubes with inhomogeneous chiralities no remarkable changes near the Fermi level occur. As intertube interaction can be neglected, the behavior of the rope coincides with that of several one-dimensional weakly interacting tubes, and so the results obtained by Ishii et al. on SWCNT mats [23] are representative of one-dimensional systems. Further evidence that the power law behavior detected by Ishii et al. [23] is related to TLL behavior has been provided by a high-resolution PES study on K-intercalated SWCNTs [4]. At low doping levels, the Fermi level of metallic tubes could be shifted away from the possible pseudo-gap region, and the same power law scaling of valence band spectrum near E_F was observed. Moreover, the authors have detected a remarkable modification of the spectral intensity at higher doping levels, which has been explained as a transition from a TLL to a FL state. Further details will be discussed later at the beginning of chapter 4. Similar results have been also achieved on Li-intercalated SWCNT bundles by Petaccia et al. [5].

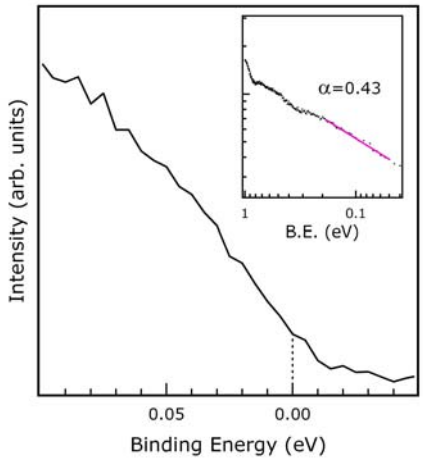

Fig. 2.1 – DOS near the Fermi level of our pristine SWCNT bucky-paper sample at T=70 K. A linear fit of the curve on double logarithmic scale and the extracted value of the α parameter have been reported in the inset.

2.2 Oxygen interaction with SWCNTs

The extreme sensitivity of both electronic and transport properties of CNTs upon gas exposure, together with their peculiar structure offering large surface areas, make the study of gas adsorption on CNTs an attractive topic for gas sensing applications [2]. Several experimental and theoretical investigations on this subject have contradicted the earliest belief, according to which nanotube electronic properties were insensitive to gas exposure. Only weak interactions between nanotubes and gas molecules were indeed expected, because of the strong C-C sp^2 bonding involving carbon atoms. It has been found instead that the electrical resistance of semiconducting nanotubes undergoes dramatic changes upon exposures to NO_2, NH_3 [51], or O_2 [52], performed at room temperature, while the removal of gas molecules (especially oxygen) from the sample produces a decrease of metallic tubes resistance [53]. An extensive theoretical study concerning the adsorption of several gases (NO_2, O_2, NH_3, N_2, CO_2, CH_4, H_2O, H_2, Ar) on SWCNTs has proved that most molecules adsorb weakly on the tubes, and that adsorption is stronger on bundles than on individual tubes. Electronic and transport properties have proved to be sensitive especially to NO_2 and O_2, due to the charge transfer and charge fluctuations [54]. Furthermore, an STS investigation has evidenced that small amounts of oxygen doping tune the local density of states of semiconducting nanotubes, which assume metallic character [52].

As far as oxygen-nanotubes interaction is concerned, some key questions are still debated, i.e. whether or not oxygen binds to SWCNTs, whether interaction occurs through physisorption or chemisorption and how it affects both electronic and transport properties of nanotubes. *Ab initio* calculations performed on SWCNTs have concluded that O_2 adsorption on SWCNTs induces p-doping of semiconducting tubes and the weak C-O coupling leads to the formation of conducting states near the band gap [55,56]. The evaluation of binding energies (0.25 eV) and charge transfer (0.1 e), resulting from calculations on O_2 interaction

with different nanotubes [55,57], seemed to support the chemical doping hypothesis. Further combined experimental and theoretical studies by Ulbricht et al. [58], concerning the kinetics of oxygen adsorption and desorption from both SWCNTs and HOPG, have showed instead that oxygen binds to these systems through weak van der Waals interactions (binding energy ≈ 0.2 eV). Moreover, the authors have found no evidence for the occurrence of strong chemical bound and dissociative adsorption. These results are consistent with previous works according to which oxygen physisorbs on graphite with a binding energy of about 0.1 eV [59]. An extensive theoretical study on oxygenation of semiconducting and metallic SWCNTs has pointed out that both O_2 physisorption and atomic oxygen chemisorption, occurring on top of the C-C bond, can modify the electronic structure of the tubes [60]. Latest density functional calculations support the conclusions of Ulbricht et al., according to which physisorption with no significant charge transfer takes place on SWCNTs [61,62]. So, it seems that the observed modifications of transport properties should be ascribed to other mechanisms.

It is worth noting that the detected sensitivity of SWCNTs to the environment conditions should be taken carefully into account, whenever the analysis of experimental investigations is carried out on supposedly pure samples, as their behavior might be strongly affected by accidental environmental gases exposure. It is well known that SWCNTs must be subjected to chemical procedures in order to remove metal catalyst particles, which have been used during the growth procedure. However, even after these purification processes there are some impurities left within the sample, that can be detected only by chemical sensitive techniques. Recent studies have accurately monitored through photoemission spectroscopy the relation between gas-SWCNT interaction and the presence of contaminants on SWCNT samples [63-65]. The results reveal that SWCNTs are very sensitive even to low concentrations of some toxic gases like NO, SO_2 and NO_2. As regards oxygen adsorption, the authors found out that it is only promoted when residual Na particles are still trapped in the bundles, as their removal can not

be achieved through mild annealing procedures. SWCNT mats subject to long-lasting annealing at 1300K are instead insensitive to oxygen exposures for pressure not higher than 10^{-6} mbar, and temperatures ranging from 150K to 300K. These findings are consistent with the occurrence of oxygen physisorption on nanotubes stated in some recent works [58,61]. So, the experimental results by Collins et al. [52], which showed the strong modifications of SWCNTs following oxygen exposure, must be explained in a different way. The observed effects should have been induced either by the presence of contaminants, or by oxygen chemisorption occurring at defect sites and open tube caps. In the last case, it is likely that high-temperature annealing yields insensitivity to oxygen exposure since structural defects have been strongly reduced [66]. These observations have highlighted that an accurate check of the sample purity degree is necessary in order to avoid misleading analysis of experimental data.

2.3 Nitrogen implantation

Physical and chemical properties of CNTs can be tuned at atomic level through substitution of carbon atoms with boron or nitrogen, carrying out a procedure usually adopted in semiconductor technology. CNTs containing N (B) atoms can be regarded as n- (p-) doped systems, as carbon has four valence electrons while N (B) has five (three) valence electrons. Calculations about nitrogen substitutional doping of both armchair and zigzag nanotubes [67] have proved that, in the case of semiconducting CNTs, the impurity gives rise to a flat energy level in the band gap, which hybridizes with the π orbitals. The result is the formation of a spatially localized state, which is chemically active, and allows the occurrence of covalent bonds between tubes and ligands or among tubes in the bundle. This phenomenon could be exploited for the realization of tunnel junction devices, since intertube bonds can modify the tunneling properties between the tubes. Further theoretical studies have proved that N-doping results in nanotubes with both

bamboo-like structure and metallic behavior [68,69]. As regards experimental methods, inclusion of nitrogen has been achieved either during the growth process in nitrogen atmosphere (via arc discharge, laser ablation, or chemical vapor deposition) or through pyrolysis process subsequent to CNT production [6,70-72]. Nevertheless, as will be discussed at the beginning of chapter 5, recent theoretical studies based on atomistic simulations [7,73] suggest that ion irradiation might be a more effective tool to achieve substitutional doping and reduce the amount of impurities bound to irregular carbon structures.

First-principles calculations show that substitutional nitrogen can significantly improve field-emission properties of CNTs, since it has one additional valence electron with respect to carbon [3]. The introduction of unsaturated dangling bond states around the Fermi level leads to a lowering of work function, a higher local DOS near E_F, and an enhanced chemical reactivity of the tip, with a consequent improvement of field-emission properties. Tight binding calculations [74] have showed that, in nanotubes with diameters smaller than 8 nm, the formation of a vacancy in the structure of CNTs is followed by reconstruction, and incorporation is achieved through chemisorption. For larger nanotubes, instead, dangling bonds are stable and N substitution occurs. The existence of a critical diameter value for N incorporation has been confirmed by experimental results on N-doped MWCNTs prepared by CVD technique.

Investigations concerning structural and electronic properties of N-doped CNTs, produced by the arc-discharge method, have evidenced the great structural disorder of the samples [6]. Moreover, it has been pointed out that nitrogen atoms bind to carbon atoms arranged either in sp^2 or irregular sp^3 configuration. An extensive XPS and EELS study on vertically aligned N-doped CNTs [75], grown by pyrolysis on silicon oxide substrates, has pointed out that the tubes have a bamboo-like structure with diameters ranging between 15 nm and 80 nm. XPS measurements performed at variable photon energies have allowed a spatial-dependent study of electronic properties, evidencing that the innermost part of nanotubes contains the

higher nitrogen concentration (about 8%). Moreover, graphite-like, pyridine like and molecular nitrogen structures have been identified: both N_2, which intercalate next to the tube inside of the tubes, and pyridine-like configuration become significant at the inner walls. Valence band spectra show that pyridine-like nitrogen concentration induces high DOS near the Fermi level, confirming previous results [76], according to which pyridine-like structure is responsible for N-doped CNT metallic behavior.

Chapter 3

Experimental apparatus and techniques

3.1 Experimental set-up

Experiments described in this thesis have been performed in the ultra-high vacuum chamber shown in fig. 4.1(a), with a base pressure of nearly $3*10^{-10}$ mbar, achieved through a pumping system consisting of a rotary-drive, a turbo-molecular, an ion and a titanium sublimation pump. The sample, a self-standing SWCNT bucky-paper by Carbon Solutions, is fastened on a tantalum window (fig. 4.1(b)) mounted on a manipulator, that allows x, y, z translations and the rotation around the main axis of the chamber. The sample can be heated up to 1400K by electronic bombardment, employing a tungsten filament facing the sample's rear side. The temperature has been controlled through a chromel-alumel thermocouple, which usually underestimates the sample temperature, as it is fixed on the sample holder; for this reason we have performed a calibration through a pyrometer with emissivity set at 100%. The upper level of the chamber is equipped with an electron gun, a conventional X-ray source, an Ultraviolet lamp, a SPECS Phoibos 100 hemispherical analyzer, a mass spectrometer, and an ion gun for gas implantation,

separated from the main body of the chamber by a metal valve. Moreover, alkali evaporation and gas exposure can be carried out making use of alkali dispensers (SAES getters), and gas inlets. Finally, a VSW HA50 hemispherical spectrometer is placed in the lower part of the chamber.

Fig. 3.1 – (a) UHV chamber (b) self-standing SWCNT bucky-paper sample

3.2 Electron Energy Loss Spectroscopy (EELS)

Low energy electron beams ($40\,eV < E < 1000\,eV$) are suitable probes for the investigation of surface electronic properties, as they strongly interact with matter and have short free mean paths (few Ångstrom) in solids. The electron penetration depth depends on energy, following the universal curve reported in fig. 3.2. Electrons show some advantages with respect to other particles for surface spectroscopy, since they are easily detectable and their energy can be tuned by devices exploiting electrostatic fields.

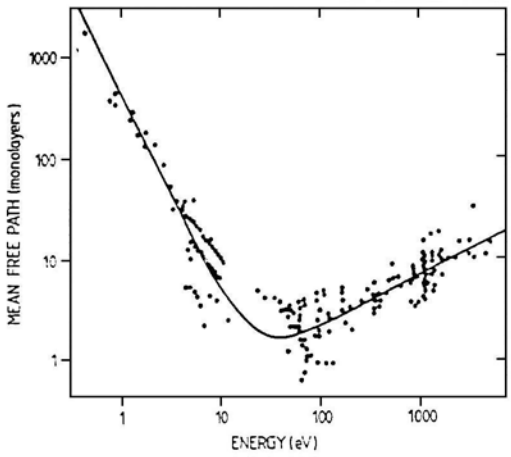

Fig. 3.2 – Electron mean free path as a function of kinetic energy

Electron Energy Loss Spectroscopy (EELS) is a technique based on the analysis of energy losses suffered by a primary electron beam as a result of its interaction with a sample [77]. In a typical EELS experiment, the distribution of backscattered electrons is detected as a function of their kinetic energy. Then, the measured intensity is usually plotted versus the energy loss suffered by the primary beam. Primary electrons which are elastically back-scattered generate a very intense elastic peak, while the loss spectrum (ranging from few meV to hundreds of eV) arises from electrons which undergo inelastic scattering, due to single- and multi-particles excitations. The main phenomena taking place at the surface region are:

- excitation of lattice vibrations (phonons) or of adsorbate vibrations;
- collective electronic excitations (plasmons);
- excitation of inter- or intra-band electronic transitions involving the valence band states;
- core level excitations.

As regards carbon nanotubes, EELS measurements have been mainly performed in transmission mode [78-80], using high-energy electrons (≈50-200 keV) which go through very thin samples and explore their bulk properties. It is worth to mention that the reflection geometry is usually employed on crystals, while some

troubles arise in the study of randomly oriented CNT bundles. In fact, the lack of a real specular direction leads to results including contributions of several transferred momenta; moreover, feasible signals are detected with respect to crystalline samples.

The theoretical treatment of the electron-solid interaction regards the electric field generated by the primary electron, which induces charge-density fluctuations in the solid. These fluctuations are related to the dielectric response of the medium to an external field, and depend on its frequency and wave vector. According to the dielectric theory, the probability per unit path that an electron undergoes an energy loss $\Delta E = \hbar\omega$ is proportional to the bulk loss function $-\mathrm{Im}\dfrac{1}{\varepsilon(\omega,\mathbf{q})}$, where $\varepsilon = \varepsilon_1 + i\varepsilon_2$ describes the dielectric response of the solid and $\mathbf{q}$ is the exchanged momentum [81,82]. This function describes the losses detected in transmission experiments, which are bulk sensitive, but provides reliable results also for EELS in reflection. Since $-\mathrm{Im}\dfrac{1}{\varepsilon} = \dfrac{\varepsilon_2}{\varepsilon_1^2 + \varepsilon_2^2}$, for a fixed value of ω the loss function exhibits maxima if $\varepsilon_1 = 0$ and ε_2 is small; this condition defines the plasma frequency, corresponding to collective electronic excitations. Core-level excitations, which are related to energy losses larger than 30 eV, usually correspond to small values of ε_2 (10^{-3}-10^{-2}) and $\varepsilon_1 \approx 1$, so that $-\mathrm{Im}\dfrac{1}{\varepsilon} \approx \varepsilon_2$ [81]. In this case, EEL spectra provide the same information as those obtained by optical absorption.

The loss function accounting for surface effects, which are remarkable in reflection geometry, is instead $-\mathrm{Im}\dfrac{1}{\varepsilon(\omega,\mathbf{q})+1}$, which has maxima for $\varepsilon_1 = -1$ and $\varepsilon_2 \approx 0$, corresponding to the excitation of surface plasmons. These collective modes propagate along the surface and are attenuated exponentially in the direction perpendicular to the surface. EEL spectra can be described by a combination of both the bulk and surface loss function, the weight of each component depending on the incidence angle and the energy of the primary electrons.

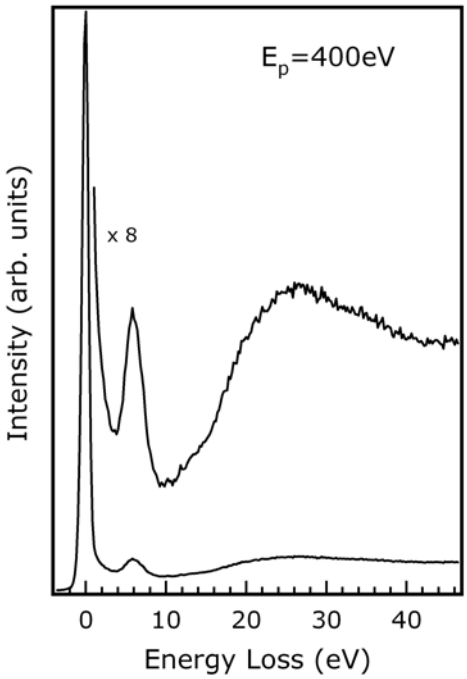

Fig. 3.3 – EEL spectrum of pristine SWCNT bundles in the loss range (0÷40)eV

In the low-energy loss range (below 50 eV), EEL spectra provide information on the individual and collective excitation of valence band electrons. We have carried out EEL measurements with energy resolution of nearly 0.8 eV, employing a primary beam energy of 400 eV and the SPECS Phoibos hemispherical analyzer. In a typical spectrum recorded in the loss range (0÷40) eV on our pristine sample, we notice a sharp peak located at 6 eV and a broad feature centered on 25 eV. These peaks, which are usually referred to as π and $\sigma+\pi$ plasmons, are related, respectively, to the excitation of a $\pi \rightarrow \pi^*$ interband transition, and of an interband transition involving π and σ valence electrons [83]. In graphite they are located at about 7 eV and 27 eV [84]; a momentum-dependent study, carried out through EELS in transmission mode, has evidenced that CNT π plasmon exhibits the same dispersion observed in graphite, so confirming the graphitic nature of nanotubes [80]. Furthermore, the occurrence of non dispersive low-energy loss peaks, corresponding to interband transitions involving vHs, has been shown.

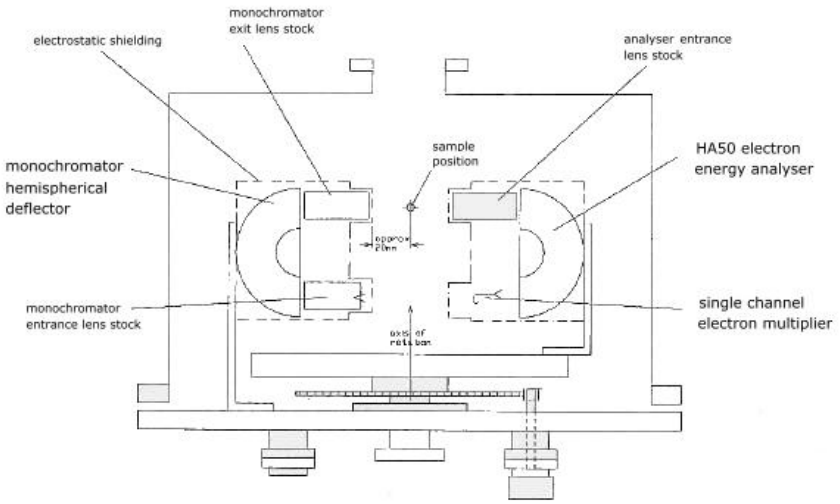

Fig. 3.4 – Scheme of VSW HA50 hemispherical spectrometer

We have used the VSW HA50 hemispherical spectrometer (scheme reported in fig. 3.5) to carry out further reflection EEL measurements employing a lower primary energy (100 eV) and a better energy resolution (80 meV). The spectrometer consists of a monochromator and a hemispherical analyzer, which is mounted on a rotating table, therefore, also angle-resolved measurements can be performed.
We have focused on the (0÷4) eV loss range, in order to detect the features located at about 0.7 eV and 1.3 eV (see clean spectrum in fig. 3.4). The two peaks correspond to interband transitions involving the first and the second couple of vHs of semiconducting tubes [84].

Furthermore, the VSW spectrometer has allowed us to make vibrational spectroscopy. High-Resolution Electron Energy Loss Spectroscopy (HREELS) exploits a monochromatized electron beam with energy lower than 40 eV and a high-resolution energy analyzer, in order to get information about very small energy losses (few hundreds of meV) due to the excitations of vibrational modes of the surface or of adsorbates present on the surface [85].

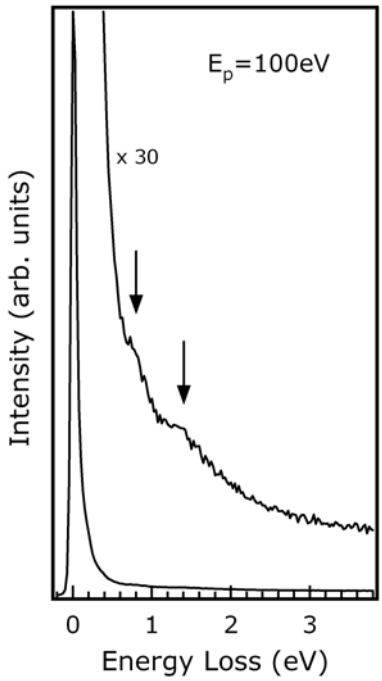

Fig. 3.5 – EELS spectrum of pristine SWCNT bundles in the loss range (0÷4)eV

With respect to optical measurements (Infrared Reflection Absorption Spectroscopy – IRAS), HREELS has a poorer energy resolution, but has a greater surface sensitivity, which allows the detection of atomic or molecular species vibrating on the surface [86]. As regards CNTs, vibrational properties are usually investigated through Raman spectroscopy (see chapter 6), which is instead a bulk technique. However, non Raman-active modes can be detected by HREELS, since Raman and HREELS have complementary selection rules, related respectively to the polarizability and the electric dipole moment. Using a primary beam energy of 30 meV and a resolution of 40 meV, we can detect two loss peaks related to CNT vibrational modes. They are located at 90 meV and 170 meV, and are assigned to a radial and a tangential CNT phonon mode, deriving from a non Raman active out-of-plane and Raman active in-plane graphite phonon mode, respectively.

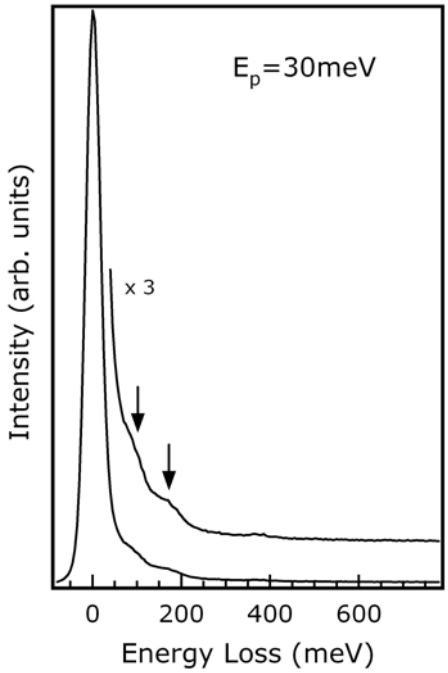

Fig. 3.6 – HREELS spectrum of pristine SWCNT bundles

3.3 Photoelectron Spectroscopy (PES)

A deeper knowledge of the electronic properties of solids can be achieved through photoelectron spectroscopy (PES), which exploits the photoelectric effect discovered by Einstein in 1905 and provides information on the electron energy distribution in a material. A photon beam produced by discrete (X-ray, U.V.) or continuous (synchrotron radiation) sources impinges on the sample, resulting in the emission of electrons (*photoelectrons*) that are detected by electrostatic analyzers. The degree of surface sensitivity depends on the energy of photoelectrons, which determines their escape depth [87].

In angle-integrated photoemission experiments only the kinetic energy of the photoelectrons is measured; the binding energy of electrons in the sample is related to the photon energy and the analyzer work function according to the equation

$$E_{kin} = \hbar\omega - \phi - |E_B| \tag{3.1}$$

In a first approximation, the behavior of photoelectron intensity versus E_B is representative of the DOS. In the case of angle-resolved PES (ARPES), photoelectrons are collected as a function of the emission angle with respect to the surface normal. Hence, this technique gives information also on the momentum of electrons in the solid and probes the band structure. As regards SWCNT bundles, ARPES can not provide useful information, since the sample consists of a disordered arrangement of tubes and has no crystallographic directions.

If X-ray sources are employed, it is possible to observe photo-ionization of the core levels, whose energies are related to the chemical state of the sample. For this reason the spectroscopy of core levels has been called also Electron Spectroscopy for Chemical Analysis (ESCA), and can be used for the quantitative analysis of chemisorbed or physisorbed species. The investigation of the valence band states requires instead high energy and momentum resolution, which can be achieved by using low photon energies, in the ultraviolet regime ($5\,eV < E < 100\,eV$). Moreover, the analysis of an UPS spectrum allows measuring the work function of the sample, which can be obtained by calculating the width of the spectral distribution between the onset of secondary electrons and the Fermi level.

As regards our measurements, we have performed X-ray and ultra-violet angle-integrated photoemission experiments with both X-rays (Al K_α line, $h\nu = 1486.6\,eV$) and U.V. (He I , $h\nu = 21.2\,eV$) sources to detect both C 1s core level and valence band spectra. The C 1s spectrum of the pristine sample, showed in fig. 3.7, is characterized by a peak located at 284.5 eV and a shake-up feature at nearly 291 eV, representing the π-plasmon excitation. It is worth noting that the disordered arrangement of bundles does not affect the peak binding energy and the C 1s line shape, in fact it has been shown in an XPS microscopy study [88] that spectra collected from a free-standing isolated bundle and a bucky-paper are very similar. The photoemission spectrum obtained employing photons in the U.V. range is instead characterized by a feature at binding energy 3 eV and a broad band centered on 8 eV, which can be assigned to π and σ states, respectively [29,83].

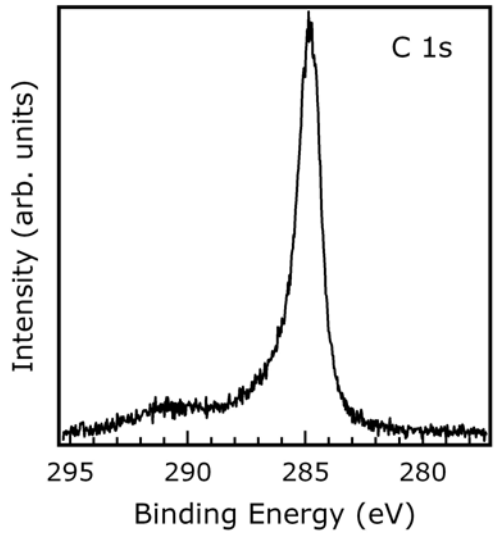

Fig. 3.7 – C 1s core level spectrum of pristine SWCNT bundles

From a detailed study of photoemission spectra we can get information on changes suffered from both chemical and electronic properties upon doping procedures. In core level spectra chemical shift or peak broadening due to modifications of the chemical environment can be detected, while changes suffered by the band structure can be pointed out in valence band spectra. In particular, it is possible to detect Fermi level shifts induced by charge transfer, and changes suffered by the DOS profile next to E_F (B.E.=0 eV) related to the transport properties of the sample.

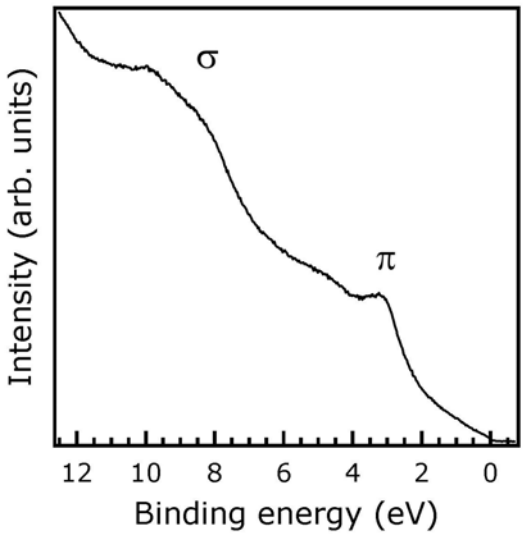

Fig. 3.8 – Valence band spectrum of pristine SWCNT bundles

Chapter 4

Sodium and lithium intercalation in single-wall carbon nanotube bundles

4.1 Introduction

Some recent studies about alkali intercalation on SWCNT bundles [4,5] deal with the low energy electronic properties as a function of doping. Rauf et al. [4] have carried out high-resolution photoemission experiments on K-doped SWCNTs and have analyzed the valence band spectra in the vicinity of the Fermi level, observing changes in the spectral shape induced by potassium intercalation. They have shown that at very low doping levels the density of states follows the power law scaling typical of the pristine sample, described by the TLL model, while at slightly higher potassium concentrations (corresponding to about one tenth of the saturation dose) the shape of the curve resembles that of metallic systems. This phenomenon has been explained as a potassium-induced transition from a one-dimensional TLL system to a three-dimensional band structure system. The authors observe a maximum Fermi level shift of about 1 eV, which determines the filling of the previously empty S_1^* and S_2^* vHs of semiconducting tubes. The resulting effect

is a transition from a sample with roughly 1/3 of metallic SWCNTs to a sample consisting of only metallic tubes, with Fermi liquid behavior. Similar results have been obtained using the same experimental technique in the study of lithium-intercalated SWCNT mats [5]. In this work, however, the increase of the density of states at E_F is observed for Fermi level shifts lower than 0.3 eV, which is not enough to achieve the filling of the first unoccupied van Hove singularity in the conduction band, located at about $E_B = 0.4$ eV. The authors suggest that the hybridization between lithium and carbon atoms could be responsible of the transition from a one-dimensional to a three-dimensional system.

In this chapter the results of both a PES and an EELS investigation concerning sodium and lithium intercalation in SWCNT bundles will be discussed, see sections 4.2 to 4.4. These experiments were meant not only to explore the behavior of sodium, which has not been previously studied, but also to investigate more widely the effects of alkali presence on the valence band states and to highlight possible different mechanisms of interaction between alkali and SWCNTs.

Finally, a photoemission study on oxygen interaction with lithium-intercalated SWCNT bundles will be presented, see section 4.5. Since it is well known [63,64] that the adsorption of oxygen, which does not occur on pure samples, is promoted by the presence of alkali metals, we further explored the mechanisms on which the interplay between oxygen and lithium atoms is based.

4.2 Experimental

Two different sets of measurements have been carried out evaporating at room temperature increasing doses of sodium and lithium on a pristine commercial SWCNT bucky-paper, which was previously cleaned through repeated cycles of annealing at 1200K. After each evaporation the absence of contaminants has been checked acquiring XPS overview spectra, while the atomic sodium (lithium) concentration has been evaluated from the ratio between the Na 1s (Li 1s) and C 1s

core edge intensities, taking into account the different photo-ionization cross sections. Since the Li 1s state has a very low cross section, doping concentrations of lithium lower than 3% could be estimated only by the evaporation length. Alkali-metal evaporations were repeated several times until the intercalation limit was reached, as revealed by the saturation of alkali concentration. Each evaporation step was followed by the acquisition of valence band, C 1s core level and medium resolution EEL spectra. UPS ($h\nu = 21.2$ eV) and XPS ($h\nu = 1486.6$ eV) measurements were performed at normal emission geometry with energy resolution set at 0.2 eV and 0.8 eV, respectively. The Fermi level calibration was carried out by measuring the Fermi edge of tantalum sample-holder. EELS measurements in the energy loss range (0÷4) eV were performed in reflection geometry with an incident angle of 45°, while the primary beam energy and the energy resolution were set to 100 eV and 80 meV, respectively. After sodium evaporations the sample was annealed at 1200 K and the complete desorption of alkali atoms and the sample purity have been checked through XPS spectra before starting with Li-intercalation experiments.

4.3 UPS and EELS measurements

Valence band spectra of both Na- and Li-intercalated SWCNTs are shown in fig. 4.1; the alkali atomic concentrations are reported next to the corresponding curves. We notice that the highest doping level achieved with sodium (2.2%) is about three times lower than that of lithium (6.0%). Moreover, for both alkali the energy position of the peak associated to the 2p-π states of valence band undergoes a shift towards higher binding energies with respect to the clean curve. The displacement measured for the 2p-π feature binding energy is due, in a rigid-band picture, to a change of the Fermi level localization induced by alkali charge transfer, so it indicates that the Fermi level position rises in the conduction band as alkali concentration increases.

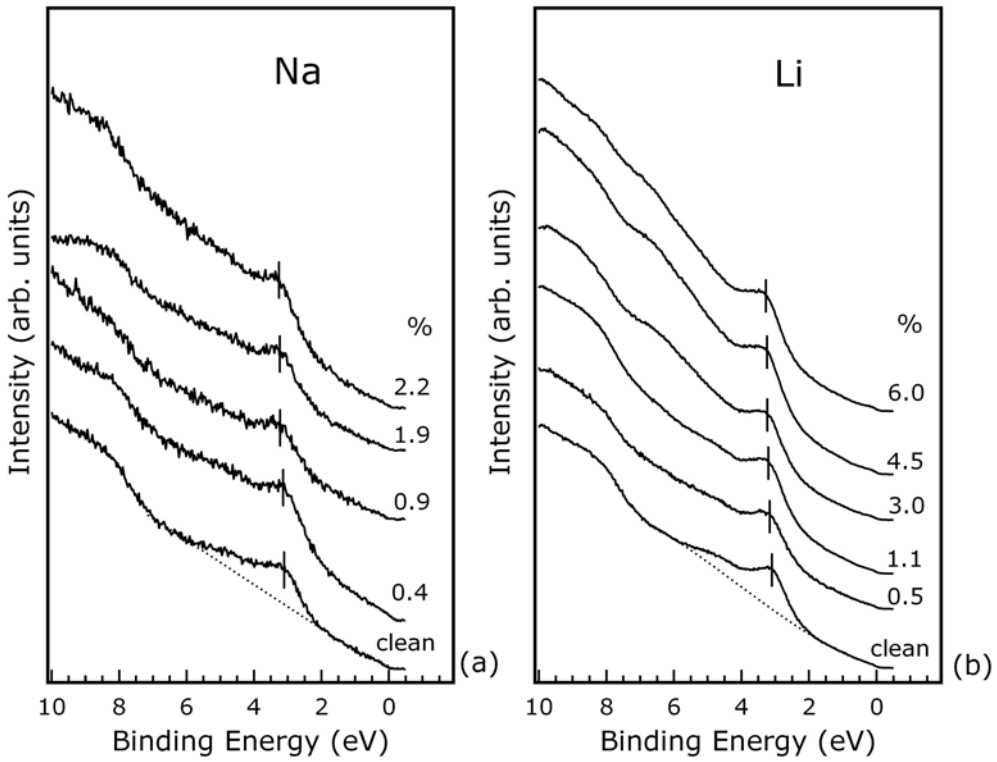

Fig. 4.1 – Valence band spectra of (a) Na and (b) Li-intercalated SWCNTs; dotted curves under the clean spectra have been used for polynomial background subtraction.

We have performed a polynomial background subtraction of each spectrum in the range $E_B=(1\div6)$ eV (dotted curves shown as example only under the clean spectra of fig. 4.1) to determine the peak shift, highlighted by the arrows in both fig. 4.2(a) and (b). The subtracted curves showed in fig. 4.2 have been normalized to the height of the main peak to better compare the spectral line-shapes. We can identify in the clean subtracted spectrum two features located at $E_B=3.1$ eV and 4.3 eV, as obtained after a Gaussian fitting procedure, and associated to 2p-π and 2p-$(\sigma+\pi)$ states, respectively. The calculated displacements of the 2p-π peak, corresponding to the sodium and lithium intercalation limit, are 0.15 eV and 0.18 eV respectively. The two alkali determine almost the same Fermi level shift at different concentrations, demonstrating, therefore, a different magnitude of charge transfer capability. In particular, lithium charge transfer is less effective than the one of any heavier alkali

atom, as shown in other works. In fact, Raman studies performed on K- and Li-doped SWCNTs indicate that, at equivalent metal concentration, Li doping determines much lower E_F values than K doping [89,90]. Furthermore, for SWCNTs doped with Li^+ by redox reactions [91] the measured Fermi level shift is significantly lower than that determined by the potassium doping at the same intercalation level [5,92].

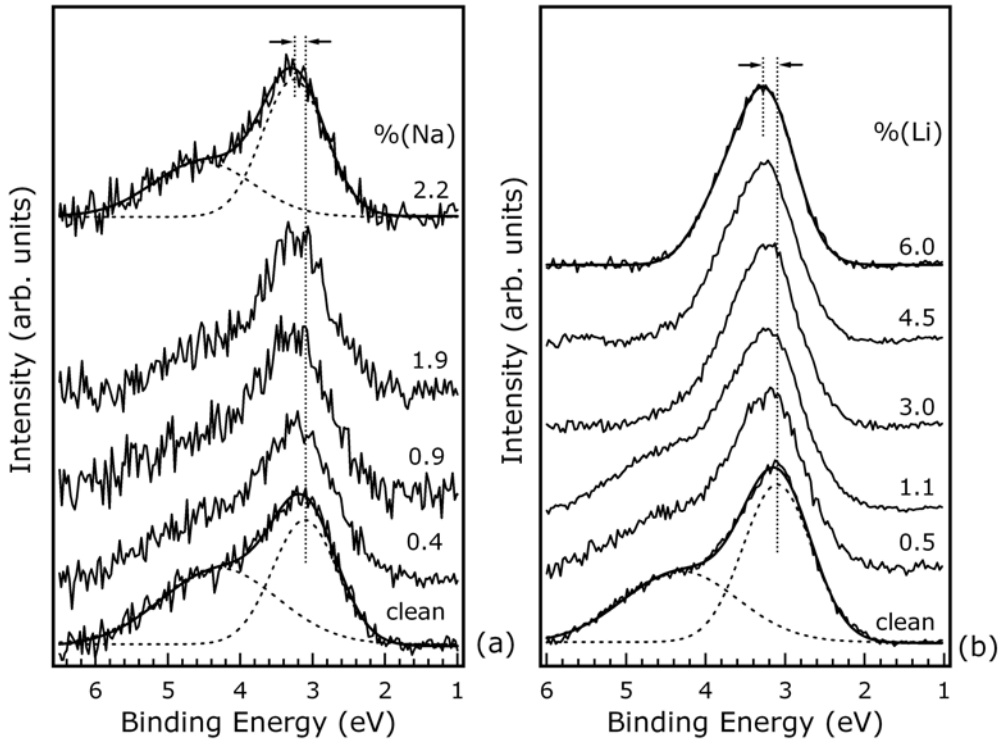

Fig. 4.2 – Valence band spectra of (a) Na and (b) Li-intercalated SWCNTs in the (1÷6)eV B.E. range after a polynomial background subtraction. Gaussian components are showed only for clean spectra and for the highest sodium dose (dashed curves)

In fig. 4.2 we observe that the feature at 4.3 eV is not affected by sodium saturation, while it gradually reduces as lithium concentration increases and completely disappears for lithium concentrations much lower than its saturation value. We argue, therefore, that the effect induced by lithium on SWCNTs band structure is related to a stronger interaction with nanotubes, which does not take place in the case of sodium.

As regards EEL spectra of Na- and Li-intercalated SWCNTs (shown in fig. 4.3(a) and (b), respectively), we have studied the behavior of the loss peaks located at 0.7 eV and 1.3 eV, related to electronic interband transitions involving the first ($S_1 \rightarrow S_1^*$) and the second ($S_2 \rightarrow S_2^*$) couple of vHs of semiconducting tubes, respectively. No evident changes occur in the spectrum as sodium concentration increases, on the contrary evident modifications are induced by lithium intercalation. Both peaks start decreasing in intensity at a doping level Li/C=0.03, and completely vanish at the maximum lithium concentration.

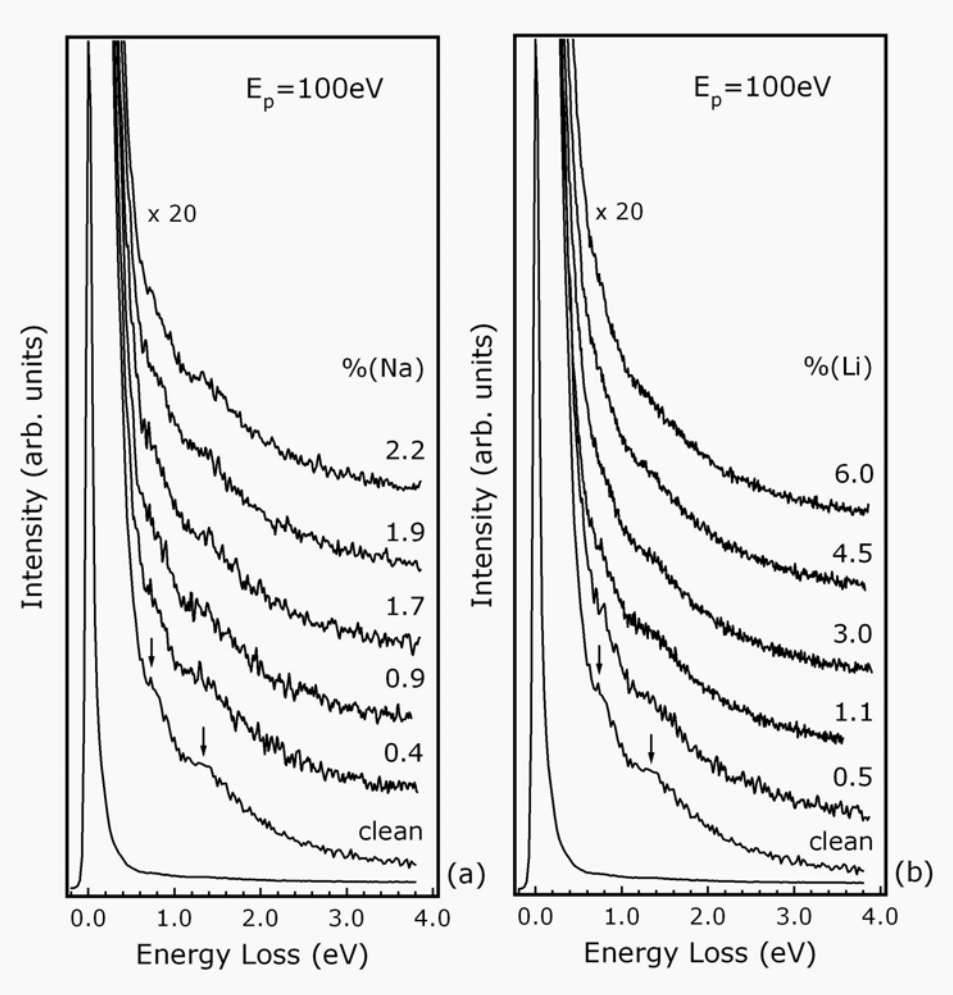

Fig. 4.3 – EEL spectra in the loss range (0÷4)eV versus (a) sodium and (b) lithium increasing concentrations. The curves have been normalized to the elastic peak height, vertically shifted, and amplified by a 20 factor to point out the two loss features

Within the framework of a rigid band model, more and more electrons are injected into the conduction band as alkali concentration increases, and, for Fermi level shifts larger than 0.4 eV, some previously allowed transition are suppressed because final states are occupied. Since gradual filling of conduction band affects at first only the lower energy states, in EEL spectra the loss peak at 0.7 eV (associated to $S_1 \rightarrow S_1^*$ transition) should disappear before than the peak at 1.3 eV, as observed by Liu and co-workers on K-doped SWCNTs [43]. As we have achieved a maximum Fermi level shift (0.2 eV) smaller than the binding energy corresponding to the first unoccupied vHs (0.4 eV), this phenomenon can not occur. The simultaneous decrease of both loss peaks intensity can be interpreted as an effect of the interaction between lithium and nanotubes. The Li-C bond seems to have covalent-like properties, as suggested by the reduced charge transfer achieved with lithium intercalation with respect to sodium. We assume that the electronic interaction among tubes in bundles is strongly enhanced by a localization of charge density along the Li-C bond, due to the covalent character of Li-C interaction. Our interpretation is supported by first-principle calculations [92] and photoemission measurements [5], both performed on Li-intercalated SWCNT bundles, according to which hybridization between lithium and carbon atoms causes the appearance of new states in the conduction band close to the Fermi level. The simultaneous vanishing of both peaks in EEL spectra can be explained as the result of a Li-induced transition from a quasi-one-dimensional towards a three-dimensional system, which determines the disappearance of vHs, peculiar of only one-dimensional systems. The suppression of the feature at $E_B = 4.3$ eV in the valence band spectra is a further evidence of the perturbation of valence band states induced by the covalent-like Li-C bond. Sodium, on the contrary, has a more effective transfer of free charge carriers which induces a Fermi level shift, but does not modify the valence and the conduction bands of SWCNTs, so that the main features of both photoemission and EEL spectra do not change upon sodium doping.

Another element supporting this hypothesis arises from the analysis of the elastic peak tail shape of EEL spectra at medium resolution. In fig. 4.4 we can look at EEL spectra corresponding to only highest sodium (a) and lithium (b) doses in comparison with the clean spectrum without any offset; in each inset an enlargement of the elastic peak tail is showed. Several theoretical and experimental studies [93-96] reported in literature have focused on the inelastic scattering involving energy losses of few meV, which are related to multiple scattering events and can be monitored through the broadening of the elastic peak of EEL spectra. According to these works, the broadening of the peak tail is linked to the existence of states near the Fermi level and to the metallic response of the conduction electrons to the long-range Coulomb fields generated by the primary electron. Semiconducting systems are therefore characterized by symmetric elastic peaks, while in the case of metallic samples the elastic peak tail is asymmetric due to the occurrence of very small losses associated to transitions between states around E_F.

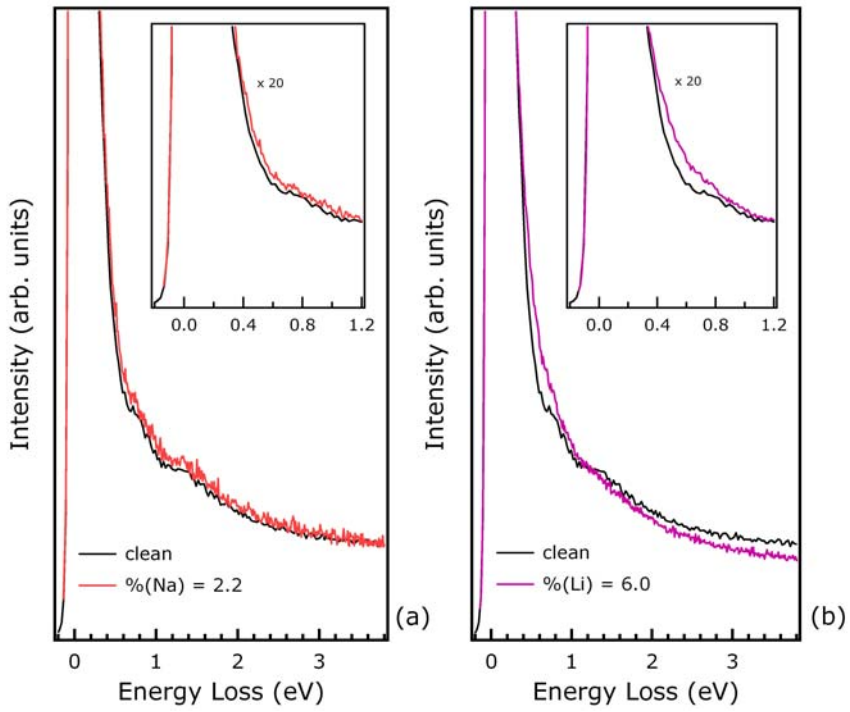

Fig. 4.4 – EEL spectra of (a) Na- and (b) Li-intercalated SWCNTs corresponding to the maximum doping level. In each inset an enlargement of the elastic peak tail range is showed.

In fig. 4.4(a) we notice that sodium does not induce substantial modifications of the line shape, while the peak tail suffers a broadening when the maximum lithium intercalation is reached. Since we have detected a Fermi level shift of 0.2 eV, the observed trend can not be ascribed to metallic tubes, which have a constant density of states in an energy range of about 1 eV centered on E_F. According to our Li-C bond picture, hybridization between atoms produces new states in the conduction band of semiconducting tubes, which should be responsible of the broadening of elastic peak at small losses. Furthermore, after exposing the Li-intercalated sample to oxygen an opposite trend occurs (fig. 4.5): the asymmetric tail is strongly suppressed and the peak shape resembles that of pristine sample.

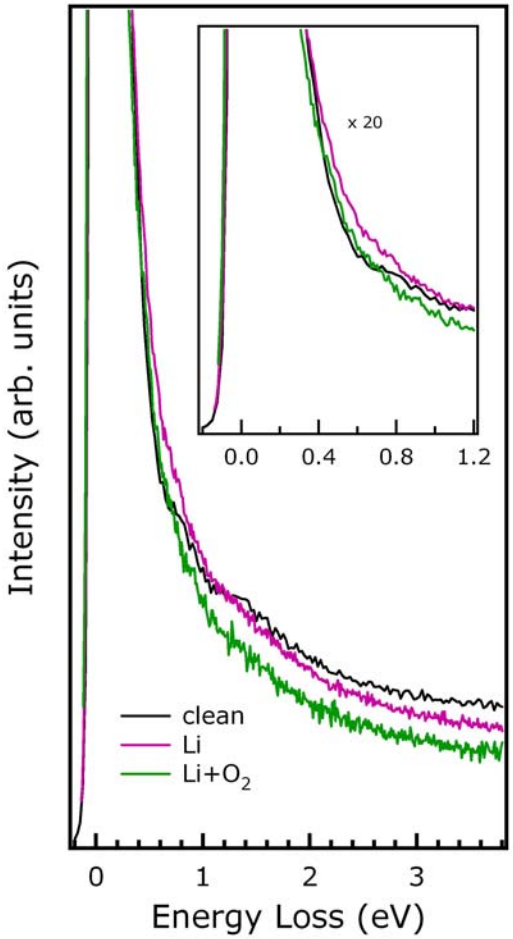

Fig. 4.5 – EEL spectra of Li-intercalated SWCNTs before and after oxygen exposure. In the inset an enlargement of the elastic peak tail range is showed.

This behavior is probably due to a weakening of the Li-C interaction induced by the formation of new bonds between oxygen and lithium atoms, as will be discussed in detail in the last section of this chapter. In the extended EEL spectrum acquired after the oxygen exposure, vHs interband transitions are not recovered, even if the elastic peak is quite similar to that of the clean spectrum. We suppose that the Li-O interplay on SWCNT surface still allows the interaction among tubes even though it leads to a strong reduction of the Li-induced hybridized states, lying just below the Fermi level. Hence, a lowering of the asymmetric tail occurs, while the system does not undergo a transition to the original one-dimensional nature and vHs interband transitions are still suppressed.

4.4 C 1s core level spectra

The C 1s core level spectrum of the pristine sample has been reported below together with the spectra corresponding to the maximum dose of sodium and lithium (fig. 4.6(a) and (b), respectively).

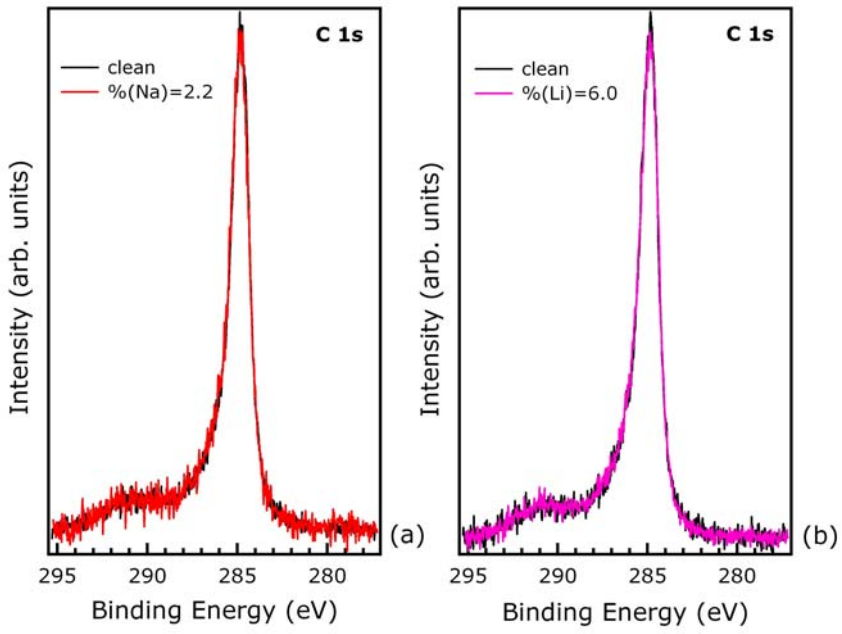

Fig. 4.6 – C 1s core level spectra of clean and (a) Na-, (b) Li-doped SWCNTs corresponding to the intercalation limit.

The peak, which is located at 284.5 eV for the pristine sample, suffered a shift towards higher binding energy after each alkali intercalation, corresponding approximately to that extracted from valence band spectra. However, the spectra have been shifted, so that the binding energy peak positions coincide, and have been normalized to the same area to emphasize changes suffered by the peak width. Sodium doping does not modify the line shape, while after Li-intercalation the peak is broadened, as can be inferred by the reduced height of the peak with respect to the clean spectrum. The measured broadening of the full width at half maximum is about 0.1 eV.

We have developed a theoretical model, based on tight binding calculations, both to describe the line shape of core level spectrum and to account for the Li-induced peak broadening. We will point out only the steps followed in the model processing, without giving a detailed account of calculations. Our aim was to clarify the role of shake-up processes, consisting in the generation of electron-hole pairs induced by the sudden creation of a core hole, which switches-on a strong local potential [87]. The contribution of conduction electrons excitations is stronger for smaller energy transfer and reaches its maximum value at the Fermi level. This is the origin of the Fermi edge singularity (FES), on which Mahan performed the first theoretical investigation [97]. In three-dimensional metallic systems the singularity, which is due to a large density of states at the Fermi level and to the presence of empty states just above E_F, is responsible of the asymmetric tail in the photoemission spectra. As for semiconducting systems, this behavior is not observed because of their quite large energy gap. XPS measurements performed on SWCNT bundles, which consist of a mixture of metallic and semiconducting tubes, reveal that the line shape of C 1s core level is quite similar to that of simple metals [98]. However, it is well known that metallic tubes have small DOS at the Fermi level, while semiconducting tubes have low energy gaps and large DOS close to E_F. As we know the mean tube diameter of our sample, we have selected metal or semiconducting bands with energy gaps below 1 eV, compatible with the allowed

chiral vectors. We can distinguish three classes of many body excitations contributing to shake-up processes, which are evidenced on the band dispersion relations in fig. 4.7:

- for metallic tubes, (i) transitions from the valence to the conduction band, both with low density of states at the Fermi level, and (ii) transitions from the valence band to an empty band of high DOS at its minimum;
- for semiconducting tubes, (iii) transitions involving two bands with high DOS close to E_F.

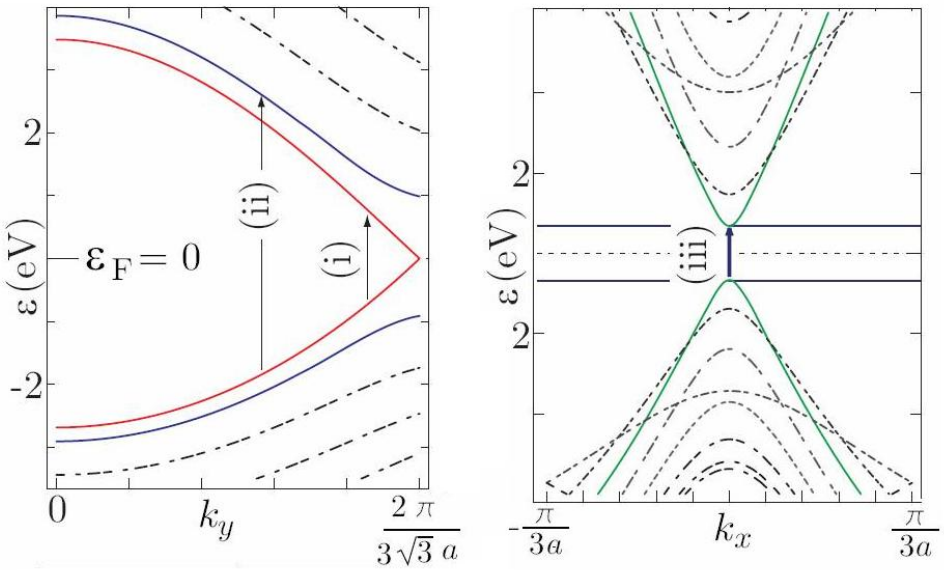

Fig. 4.7 – Band dispersion relations of metallic (10,0) and semiconducting (16,0) tubes. The competing shake-up mechanisms illustrated in the text are reported (i-ii-iii).

All the processes listed above contribute to shake-up, although (ii) and (iii) give rise to an asymmetric distribution displaced from the threshold by the energy gap of semiconducting tubes. We have found that the XPS spectrum is constituted by two components: the main symmetric peak accounts for electrons remaining in the ground state, while the asymmetric contribution is related to the energy distribution of shake-up electrons (S) originating from both metallic and semiconducting tubes.

Then, the S-distribution for the (10,10) and (16,0) tubes has been calculated and a function containing both components has been constructed to fit the C 1s core-level spectra. We have found that the energy shift between the main peak and the maximum of the asymmetric distribution is 0.8 eV, which corresponds approximately to the semiconducting gap value of our sample. This result points out that (iii) couplings give the main contribution to shake-up processes, as they involve high DOS states. The value of the asymmetric index (α), obtained after the fit procedure, has been reported next to each spectrum in fig. 4.8. The α parameter, on which the energy distribution of shake-up electrons depends, is related to the response of different electronic structures and ranges typically from 0.1 to 0.3 in the case of simple metals [87].

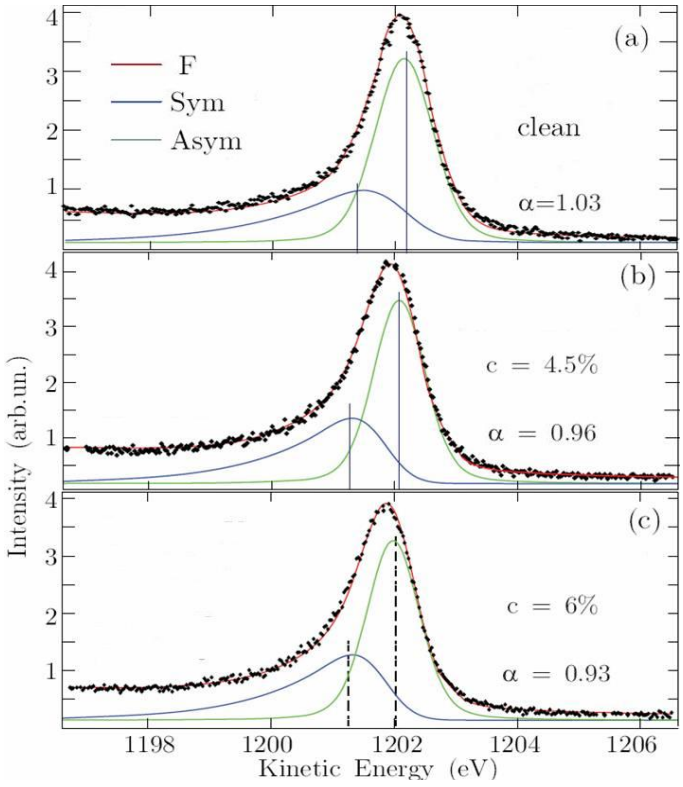

Fig. 4.8 – C 1s spectra and fit-curve of (a) clean and (b)-(c) Li-doped SWCNT bundles.

The asymmetric index, which is larger than 1 for the clean spectrum, shows a trend toward lower values with increasing lithium concentrations, indicating a more significant contribution of small energy transitions near E_F. This behavior can be explained if we take into account that, as the Fermi level rises in the conduction band, states with a higher DOS can be involved in (i) and (ii) couplings of metallic tubes, thus leading to a significant enhancement of shake-up electrons near the threshold.

However, also our hypothesis on Li-C covalent-like interaction can provide an explanation of the observed α decreasing trend. The presence of new hybridized states in the energy region corresponding to the semiconductors gap can indeed contribute to an increase of shake-up electrons, through (iii) couplings. These mechanisms involve states with a very high DOS (vHs), and so can strongly influence the asymmetric component of the XPS spectrum. In conclusion, we have found that the broadening of the C 1s spectrum with increasing Li intercalation is consistent with our interpretation of both EELS and UPS measurements.

4.5 Oxygen on Li-intercalated SWCNT bundles

Oxygen interaction with Li-intercalated SWCNT bundles has been investigated by photoemission spectroscopy; we have compared the behavior of the O 1s core-level and valence band spectra versus oxygen exposures and thermal treatments. All the O 1s and Li 1s core level spectra have been Shirley-type background subtracted and normalized to the area of the corresponding C 1s spectrum to put in evidence the concentration changes. In fig. 4.9(a) the bottom curve is the O 1s spectrum of the clean sample: a residual amount of oxygen (1%) is irreducible even after several annealing procedures at 1200K. Since oxygen does not adsorb on a perfectly pure SWCNT sample [63], this effect is likely induced by the presence of some catalytic particles, which have not completely desorbed.

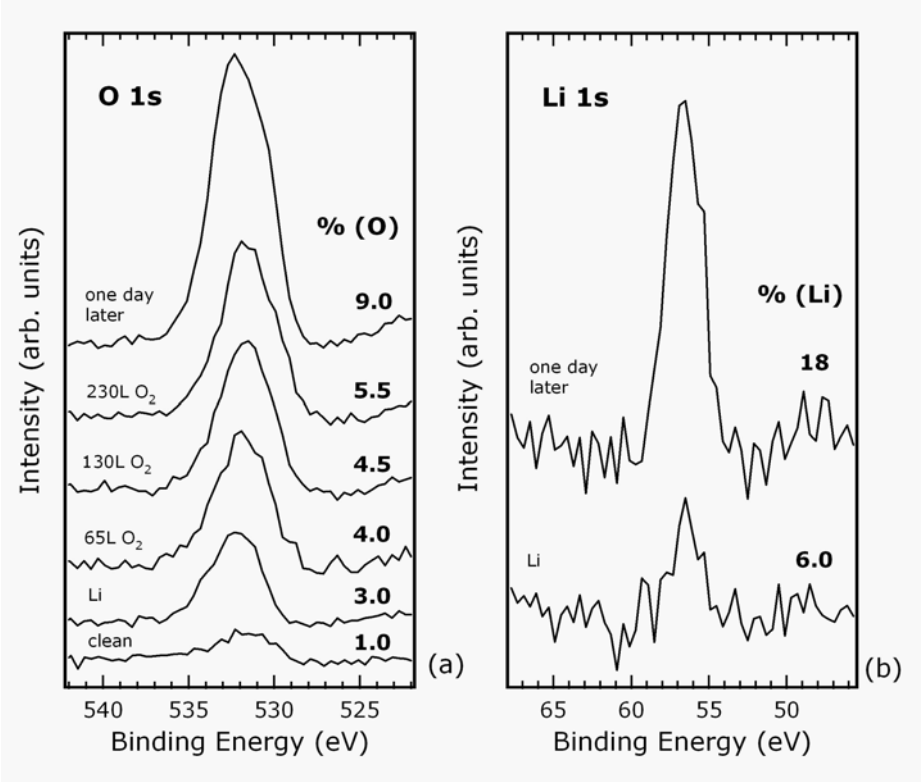

Fig. 4.9 – (a) O 1s and (b) Li 1s core level spectra of Li-intercalated SWCNT bundles for increasing oxygen exposures. Upper curves have been acquired one day later with respect to the last exposure.

The atomic concentrations, detected after reaching the Li intercalation limit at room temperature (see "Li" curves in fig. 4.9), were 6% for lithium and 3% for oxygen, the increased amount of the latter being caused by an enhanced reactivity of the sample induced by the alkali. Oxygen concentration grew up to 5.5% after three exposures at increasing doses. A surprising effect was noticed acquiring the spectra one day later: in fact, without having performed further exposures or evaporations, we have detected an oxygen concentration of about 9.0%, and a remarkable increase of lithium concentration from 6% to 18% (top curve of fig. 4.9(b)). Moreover, the O 1s peak suffered a broadening and a small shift toward higher binding energies with respect to the former value, which was approximately 532 eV.

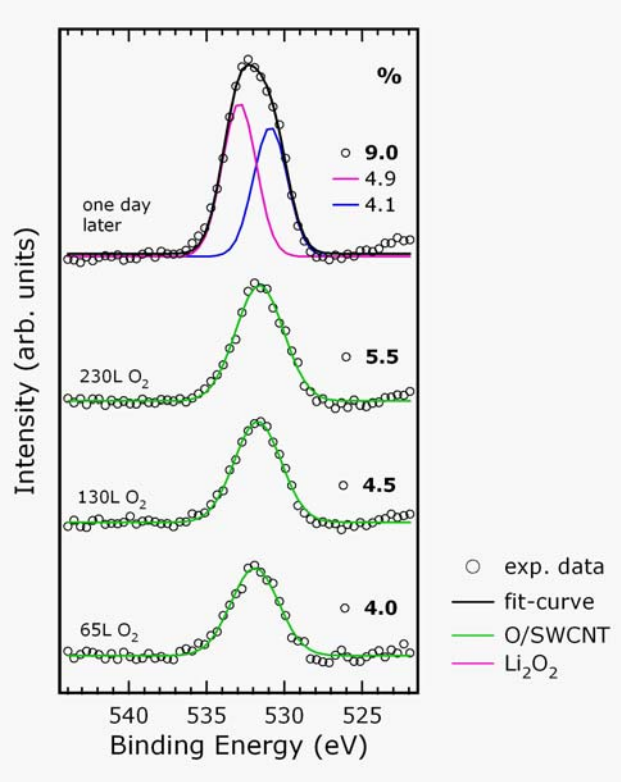

Fig. 4.10 – Gaussian fitting results of O 1s core level spectra of fig. 4.9(a); the total and partial concentrations are reported next to each curve.

We carried out a Gaussian fitting procedure on the O 1s spectra (fig. 4.10), obtaining that for oxygen concentrations up to 5.5% there is only one component located at 532 eV, associated with oxygen adsorbed on nanotubes (alkali-induced adsorption). The best-fit curve of the last spectrum is achieved instead with two peaks located at 531 eV and 533 eV, which can be assigned, respectively, to oxygen belonging to lithium oxide (LiO_2) and peroxide (Li_2O_2) [99,100]. So, we suppose that electronegative oxygen atoms attract lithium atoms from the bulk, leading to a dramatic increase of lithium concentration in the surface region, on which the formation of both LiO_2 and Li_2O_2 occurs. The concentration of both components has been evaluated with respect to the C 1s spectrum area and is reported next to each curve in fig. 4.10, 4.11, and 4.12.

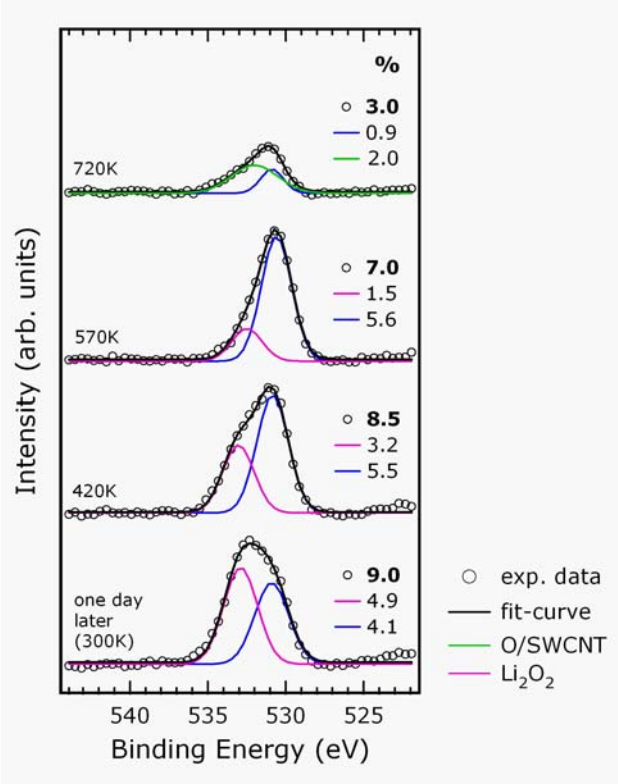

Fig. 4.11 – Gaussian fitting results of O 1s core level spectra; the total and partial concentrations are reported next to each curve.

The spectra reported in fig. 4.11 and 4.12 concern a further study, that we have carried out to investigate the temperature-induced effects on the O 1s line shape. Annealing at 420K lead to a slight reduction of oxygen and lithium atomic concentration (from 18% to 16%, and from 9% to 8.5%, respectively); regarding the two oxygen components, lithium oxide increased at expenses of lithium peroxide. A successive annealing step at 570K did not affect the Li_2O component, while determined a decrease of Li_2O_2. Hence, we notice that lithium peroxide is the less stable compound, since it is reduced just after a soft annealing. Lithium and oxygen concentrations were strongly suppressed upon heating at 720K: they were reduced in fact to about 5% and 3%, respectively. In particular, in the O 1s spectrum, the Li_2O_2 component vanished and only a residual of lithium oxide was still present, while the main contribution was due to the O/SWCNT component.

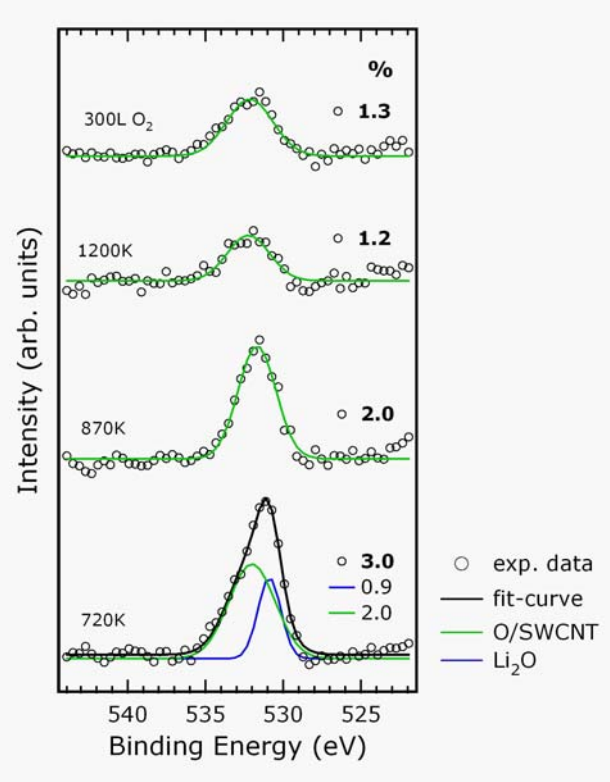

Fig. 4.12 – Gaussian fitting results of O 1s core level spectra; the total and partial concentrations are reported next to each curve

After heating the sample at 870 K, the lithium-oxygen compound components completely vanished and only 2% of both oxygen and lithium, each independently interacting with the sample, were still present. Upon heating at 1200 K, lithium completely desorbed and the usual irreducible 1% of oxygen was detected. Finally, the topmost curve of fig. 4.12 confirms that oxygen adsorption does not take place on a real clean sample, as already reported in literature.

Also UPS measurements confirmed the presence of both lithium oxide and peroxide molecules, as shown in fig. 4.13(a). Lithium intercalation induces a shift of the π band from 3 eV ("clean" curve) to 3.2 eV ("Li" curve), as already discussed in section 4.3; then, the early position is gradually recovered upon annealing, due to lithium desorption from the sample.

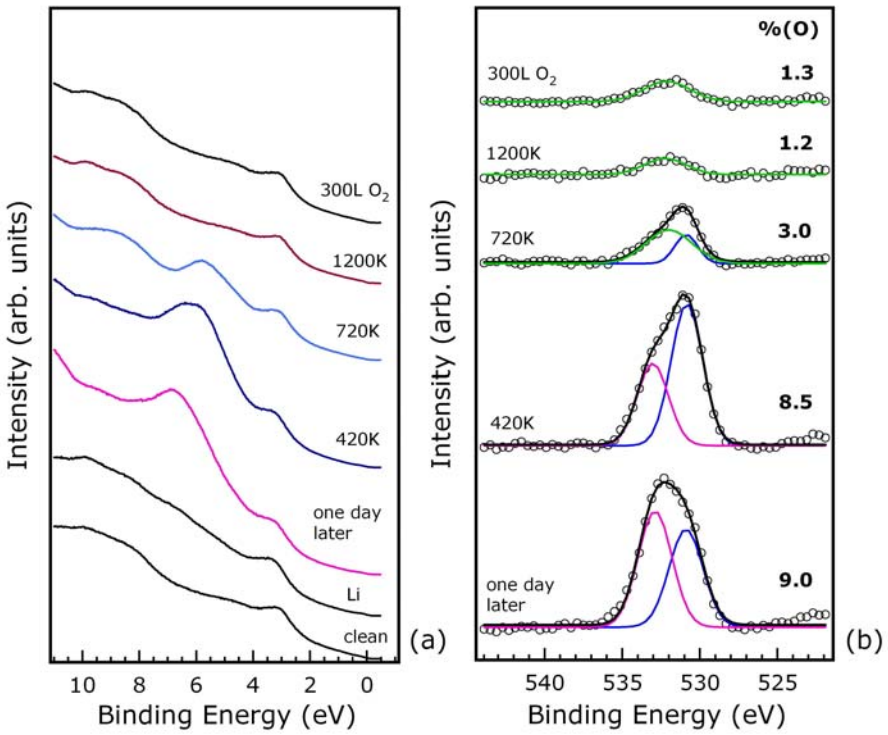

Fig. 4.13 – (a) Valence band spectra of clean and Li-intercalated SWCNT bundles exposed to oxygen and then gradually heated (b) The corresponding O 1s spectra

On the "one day later" curve (the third from the bottom in fig. 4.13(a)), corresponding to a situation in which lithium peroxide is the main species, a new broad feature centered at about 7 eV is present. After annealing at 420 K, when lithium oxide becomes the main component in the O 1s spectrum, the new feature suffers a shift towards 6 eV, and reduces in intensity after a further annealing at 720 K. The pristine valence band spectrum is recovered only after annealing at 1200 K. As oxygen does not adsorb on the clean sample, the valence band spectrum does not change at all; this behavior is consistent with the previously discussed XPS results. The modifications involving these new features can be better observed on the background-subtracted curves reported in fig. 4.14 in the binding energy range (2÷11) eV; in the inset an example of the polynomial background curve is shown.

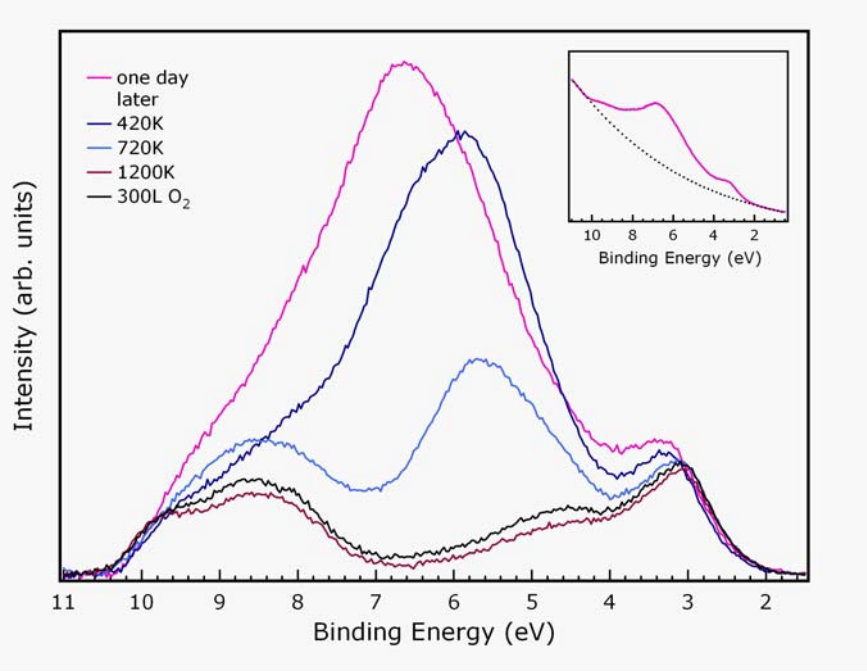

Fig. 4.14 – Valence band spectra in the (2÷11) B.E. range after background subtraction. In the inset an example of the polynomial background curve is shown.

The broad feature centered on 7 eV in the pink curve of fig. 4.14 results from the superposition of the σ band and of two peaks located at nearly 5.5 eV and 8.5 eV. According to previous results concerning the study of Li-O interaction [99], we assign these features to LiO_2 and Li_2O_2, respectively. Therefore, the shift toward 6 eV after the annealing at 420 K confirms that LiO_2 has become the main species. After reaching 720 K, the peak intensity is remarkably decreased, due to the partial LiO_2 desorption, while the σ band can be now clearly identified at approximately 8.5 eV because of the lithium peroxide component vanishing. The observed valence band spectra behavior is therefore consistent with XPS results, confirming that the formation of lithium oxide and peroxide takes place on the sample surface.

4.6 Conclusions

Intercalation of SWCNT bundles with sodium and lithium atoms, performed at room temperature, allowed us to better understand the different mechanism of interaction of each alkali with nanotubes. UPS, EELS [101] and XPS [102] measurements revealed that sodium doping induced only a Fermi level shift due to charge transfer, while it did not affect the valence and conduction band states and the C 1s core level of SWCNTs. Sodium atoms seem therefore to contribute only to an increase of charge carriers without interacting with nanotubes, which keep their electronic properties unchanged. On the contrary, lithium induces striking changes of valence and conduction band states and this behavior suggests the existence of hybridized states due to the formation of covalent-like bonds. The formation of links among tubes leads to a transition from a one- to a three-dimensional system, evidenced by the suppression of interband transitions between vHs of semiconducting tubes. This interpretation is also supported by a lithium-induced C 1s core level broadening, which is compatible with the formation of new states in the gap-region of semiconducting tubes.

Photoemission measurements on Li-intercalated SWCNT bundles exposed to oxygen at room temperature have revealed the occurrence of chemical reactions between lithium and oxygen atoms on the sample surface. The enhanced sample reactivity, caused by the alkali presence, allows the adsorption of oxygen, which in turn induces a remarkable de-intercalation of lithium atoms from the bulk. This process, which does not occur immediately, results in a strong increase of the lithium surface concentration, and is followed by the formation of both lithium peroxide and oxide. Moreover, a temperature-dependent study has showed that lithium peroxide has a less stable bond than lithium oxide and starts desorbing at 400K; at temperatures higher than 1000K both oxygen and lithium desorb, and the electronic structure of the pristine sample is recovered.

Chapter 5

Nitrogen ion implantation in single-wall carbon nanotube bundles

5.1 Introduction

In the last years, several methods have been developed to realize implantation of nitrogen impurities in carbon nanotubes. This doping technique is very attractive since nitrogen atoms, having roughly the same atomic radius and one more valence electron than carbon atoms, are capable of both occupying substitutional sites and modifying CNT electronic properties. However, if doping is carried out through arc-discharge techniques or substitutional reactions, only small amounts of N atoms have been found to reside in the substitutional sp^2 configuration in the nanotube atomic network. Actually, most of nitrogen impurities chemisorb on the CNT surface, or intercalate in the form of molecular nitrogen, or bind to sp^3 irregular sites [6,71,103]. Moreover, according to theoretical calculations [74], substitutional reactions are unlikely to occur for CNTs with diameters smaller than 8 nm, as already mentioned in chapter 2. Recent atomistic computer simulations [7,73] have revealed that ion irradiation, which is routinely used in

semiconductor technology, might be a more efficient method to achieve nitrogen substitutional doping. Until now, N^+ ions have been implanted into graphite and fullerene solids [104,105], but not in carbon nanotubes. The simulation of both B and N irradiation has showed that up to 40% of the impinging ions can directly occupy the sp^2 sites and that this amount can increase upon thermal treatments. Annealing can indeed induce a higher mobility of dopant species, that can be rearranged via diffusion and undergo incorporation at vacancies. Moreover, it has been proved that the best value of energy, which optimizes the efficiency of substitutional doping, is approximately 50 eV. Since these theoretical results suggest that irradiation-mediated doping is a promising technique, we have planned to carry out N_2^+ ion-implantation in SWCNT bundles. As no previous experimental results about the real effectiveness of this method can be found in literature, we have used a high energy (3 keV) ion beam to estimate the achievable nitrogen atomic concentrations, and then we have performed an extensive analysis of chemical and electronic properties of N-doped samples, as a function of either nitrogen dose or temperature.

5.2 Experimental

Nitrogen implantation has been carried out at room temperature collimating 3 keV N_2^+ ions, produced with a cold cathode ion source, at normal incidence on the SWCNT bucky-paper sample, which was previously cleaned through repeated cycles of annealing at 1200 K. The beam was rastered over the whole surface area and the typical ion current density was $1 \cdot 10^{12}$ ions/cm$^2 \cdot$ s. Three implantation procedures have been performed, corresponding to a dose of about $1 \cdot 10^{15}$, $2 \cdot 10^{15}$ and $4 \cdot 10^{15}$ ions/cm^2, respectively. The implantations will be referred to as i1, i2, and i3 hereafter. Both i1 and i2 were followed by an annealing at 1200 K (a1 and a2, respectively), while after i3 the sample was annealed by step at 650 K, 800 K, 1000 K

and finally 1200 K (a3). The sample temperature was monitored with an optical pyrometer with emissivity set at 100%. N 1s and C 1s core levels, EEL, HREEL and valence band spectra were taken after each implantation or annealing.

Photoemission measurements (XPS: hν=1486.6 eV - UPS: hν=21.2 eV) have been performed at normal emission geometry. N 1s and C 1s spectra have been collected with a constant pass energy of 15 eV and nitrogen atomic concentration has been evaluated from the N/(N+C) ratio, taking into account the photo-ionization sensitivities. Since the mean free path of both C 1s and N 1s photoelectrons is comparable to the N implantation depth, the calculated concentrations can be roughly considered as the atomic ratio in the probing region of about a few tens of Å. C 1s core level spectra showed in fig. 5.2 have been acquired at a higher resolution (FAT=6 eV), to better evaluate the broadening of the peak. At this low pass energy, the energy resolution (≈ 1 eV) is the same of the X-ray source. UPS measurements were carried out with an energy resolution of 0.2 eV, and the Fermi level calibration was realized by measuring the Fermi edge of tantalum sample-holder. Both EEL and HREEL measurements have been performed in reflection geometry; spectra in the energy loss range (0÷40) eV and (0÷4) eV have been taken setting the primary beam energy and the energy resolution at (400 eV, 0.8 eV) and (100 eV, 80 meV), respectively. As regards HREEL measurements, the incidence angle, the primary beam energy and the energy resolution were 45°, 30 eV, and 40 meV, respectively.

5.3 Chemical properties: XPS and HREELS measurements

The chemical structure of N-doped SWCNT bundles has been investigated both by XPS and vibrational spectroscopy (HREELS); we have analyzed the behavior of the N 1s and C 1s core-level spectra versus increasing nitrogen doses and thermal treatments. All curves have been Shirley-type background subtracted. The spectra shown in fig. 5.1(a) have been normalized to the height of low binding

energy peak, to emphasize line shape variations; the curves of fig. 5.1(b) have been normalized instead to the area of the corresponding C 1s spectrum, to put in evidence the increase of concentration.

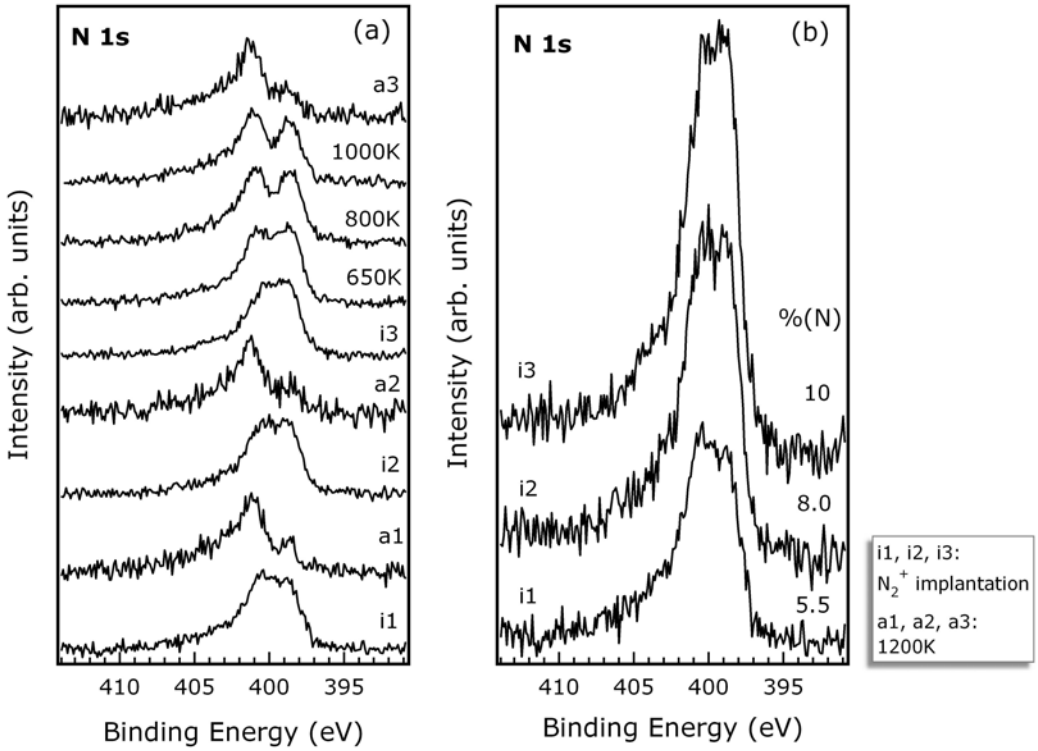

Fig. 5.1 – N 1s core level spectra (a) curves normalized to the height of the peak at higher B.E (b) curves acquired after ion irradiation, normalized to the area of the corresponding C 1s spectra.

We note that i1, i2, and i3 spectra, corresponding to atomic nitrogen doses of about 5%, 8% and 10%, respectively, are structured. A peak located at about 402 eV and a residual component around 398 eV can be distinguished after annealing the sample at 1200 K. The thermal treatments carried out after i3 point out the gradual modifications suffered by the line shape. The component at low B.E. nearly vanishes at the last annealing step at 1200 K, and the a3 curve resembles the shape of both a1 and a2 spectra. We have performed a detailed analysis of these spectra,

fitting them with a set of Gaussian curves; each component corresponds to a different coordination of nitrogen atoms, as will be discussed in the next section.

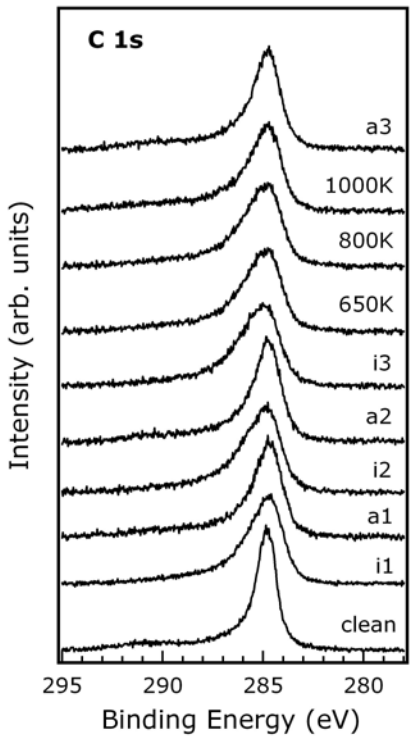

Fig. 5.2 – C 1s core level spectra

As regards C 1s core level spectra, we notice in fig. 5.2 that nitrogen implantation induces a broadening of the peak from 1.1 eV (clean) to about 2 eV. This effect can be due to the structural disorder produced in the carbon network by ion irradiation, but also to the modified chemical environment consequent to nitrogen incorporation. The main peak located at 284.5 eV represents the graphite-like C-C bond, while contributions at slightly higher binding energies are related to carbon atoms bound to nitrogen in different configurations, as reported by Jang et al. [72]. The width of the peak decreases upon annealing, and reaches about 1.5 eV at the highest temperature, but the width of the clean sample is never restored. We will see in next sections that none of the electronic properties is indeed entirely

recovered after annealing at 1200 K, indicating that ion bombarding has induced a permanent alteration of the nanotube network.

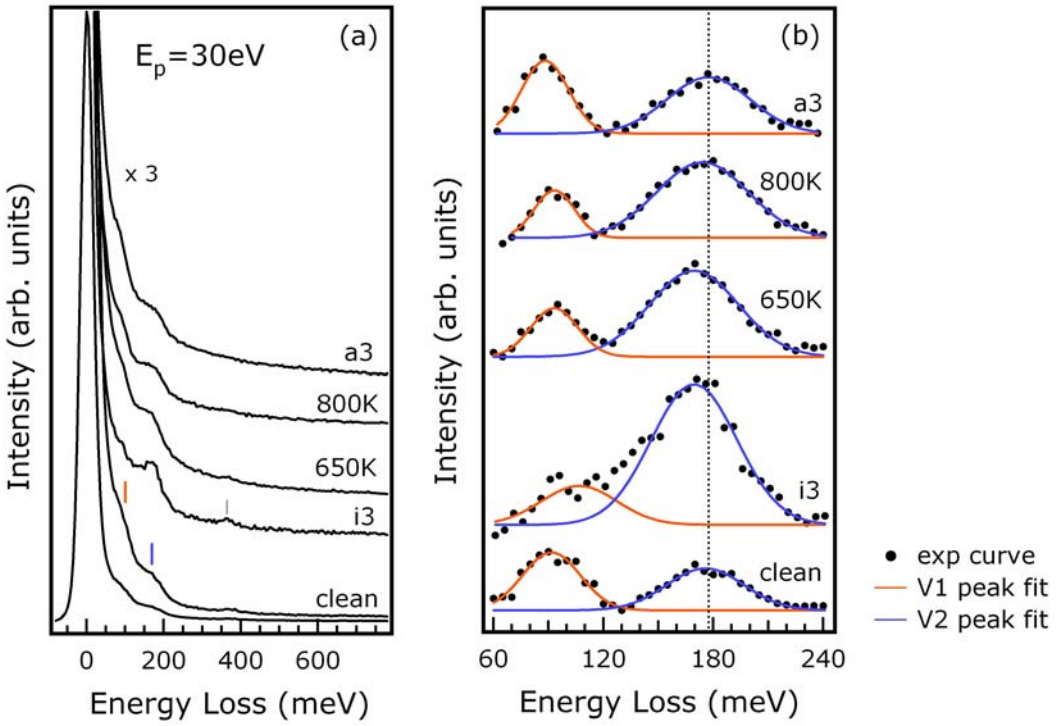

Fig. 5.3 – (a) HREEL spectra of clean, N-implanted (maximum N dose) and annealed SWCNT bundles. The spectra have been normalized to the elastic peak height, vertically shifted, and amplified by a 3 factor. (b) The same curves after background subtraction in the loss range (60÷240) meV.

Further data concerning the chemical properties of the sample have been obtained through HREEL measurements (fig. 5.3(a)). We have performed a smooth background subtraction of each curve to best follow the modifications suffered by the main peaks in the energy loss range (60÷240) meV (see fig. 5.3(b)), which are located at 90 meV (V1) and 180 meV (V2), and are assigned to a radial and a tangential phonon mode, respectively (see chapter 3). After nitrogen implantation, both the strong reduction of the component V1 and the presence of the loss peak at 360 meV, correlated to C-H stretching vibration, indicate the increase of structural disorder. In fact, hydrogen atoms can easily bind with defects, i.e. unsaturated

dangling bonds, induced by ion irradiation. We further notice that V2 peak rises in intensity, broadens and shifts toward lower energy (≈ 170 meV) upon irradiation. This energy loss value is assigned to C-N stretching [10], but also N-H and N-O contribution are present (as oxygen adsorption is favored by the defects presence). The intensity of C-H loss peak gradually lowers versus increasing annealing temperature; at 1200 K it vanishes, while the V2 peak shifts backward and the V1 recovers its previous intensity, indicating the desorption of nitrogen atoms and a fine restoring of the nanotube structure.

5.4 Analysis of N 1s spectra

The results of the multi-peak Gaussian fit of the N 1s core level spectra are showed in fig. 5.4, 5.5, and 5.6. All the curves have been normalized to the area of the corresponding C 1s spectra, to emphasize the concentration changes for total and partial nitrogen components (the total concentration has been evaluated from the experimental curve). We identify three main peaks, with nearly the same FWHM (1.8 eV), located at B.E.=398.7(±0.1) eV, 400.3(±0.1) eV and 401.3(±0.1) eV. According to previous results concerning synthesized CN_x nitrides [107], nitrogen implantation in graphite and N-doped CNTs, these features can be attributed to nitrogen atoms bound in tetrahedral sp^3 (N_1-see fig. 5.4), in sp^2 pyridine-like (N_2), and sp^2 graphite-like configuration (N_3), respectively. N_2 defect-related feature correspond to nitrogen atoms bound at the edge of disrupted nanotubes or defective tubes, and is associated to defects of the nanotube structure as well as sp^3 atoms (N_1); N_3 is the most significant component, since it is related to nitrogen atoms placed in sp^2 substitutional sites.

A further broader component N_4 (FWHM = 4.2 eV) must be added, to take into account contributions coming from nitrogen atoms bound to oxygen impurities; the corresponding concentration has not been reported in the figures, as it is always smaller than 2% and it is not much relevant for our analysis.

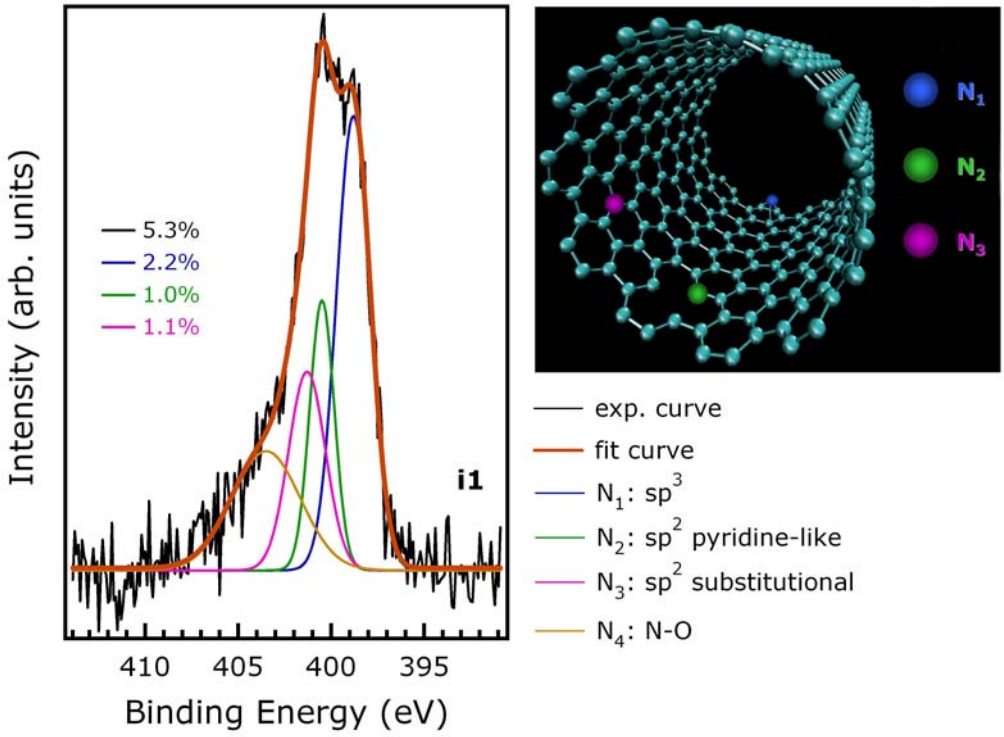

Fig. 5.4 – Gaussian multi-peak fitting of the N 1s core level spectrum after the first N_2^+ implantation; all curves are normalized to the area of the corresponding C 1s core level spectrum. The N atoms configurations related to the components are showed in the picture. The total and the partial N atomic concentrations are reported next to the spectrum.

Nevertheless, we have verified that oxygen atomic concentration slightly increases upon ion irradiation from the irreducible 1% of the clean sample to 1.5%. This behavior is likely due to the production of defects, induced by ion irradiation, which in turn enhances the reactivity of the sample. Annealing produces a partial restoring of the structure and a consequent desorption of oxygen itself.

If we compare the i1, i2 an i3 spectra, we notice that the three components rise as the nitrogen dose increases and that N_1 suffers the maximum growth; this can be easily explained if we consider that, for more lasting irradiation time, a greater number of defective sites is produced. After the annealing at 1200K, instead, the spectra are essentially the same, irrespective of the different initial status.

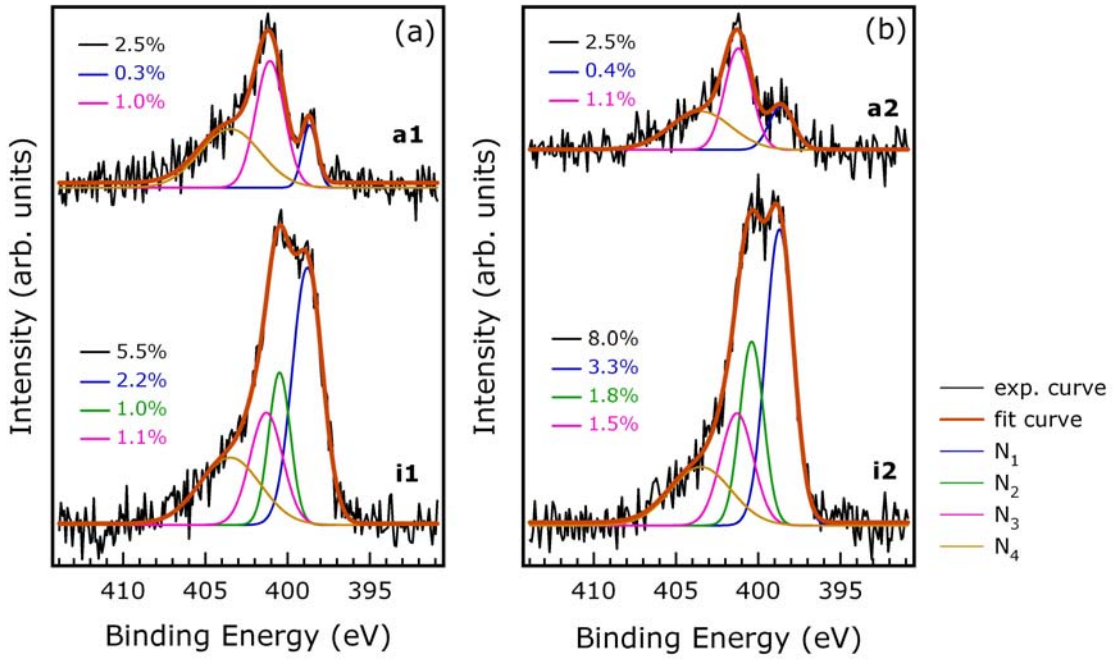

Fig. 5.5 – Gaussian multi-peak fitting of the N 1s core level. All curves are normalized to the area of the corresponding C 1s core level curve. The total and the partial nitrogen atomic concentrations are reported next to each spectrum.

It is worth noting that in both cases about 1% of substitutional nitrogen is not affected by thermal treatment, while a negligible amount of sp^3 nitrogen is still detected and pyridine-like component is vanished. The gradual thermal treatments performed after i3 implantation provide further information on the different bonding configurations. The annealing at 650K leaves the total N concentration almost unchanged, moreover substitutional nitrogen grows at the expense of pyridine-like component and reaches its maximum value (about 2.5%). This behavior confirms the prediction of simulations performed by Kotakoski et al [7], according to which annealing can promote a higher mobility of nitrogen impurities. So, they likely find other vacancies and recombine with them, with a consequent increase of sp^2 substitutional doping. Also a partial recovering of the structure, which induces a conversion of some sp^2 defects into substitutional sites [104], can account for this rearrangement of nitrogen atoms.

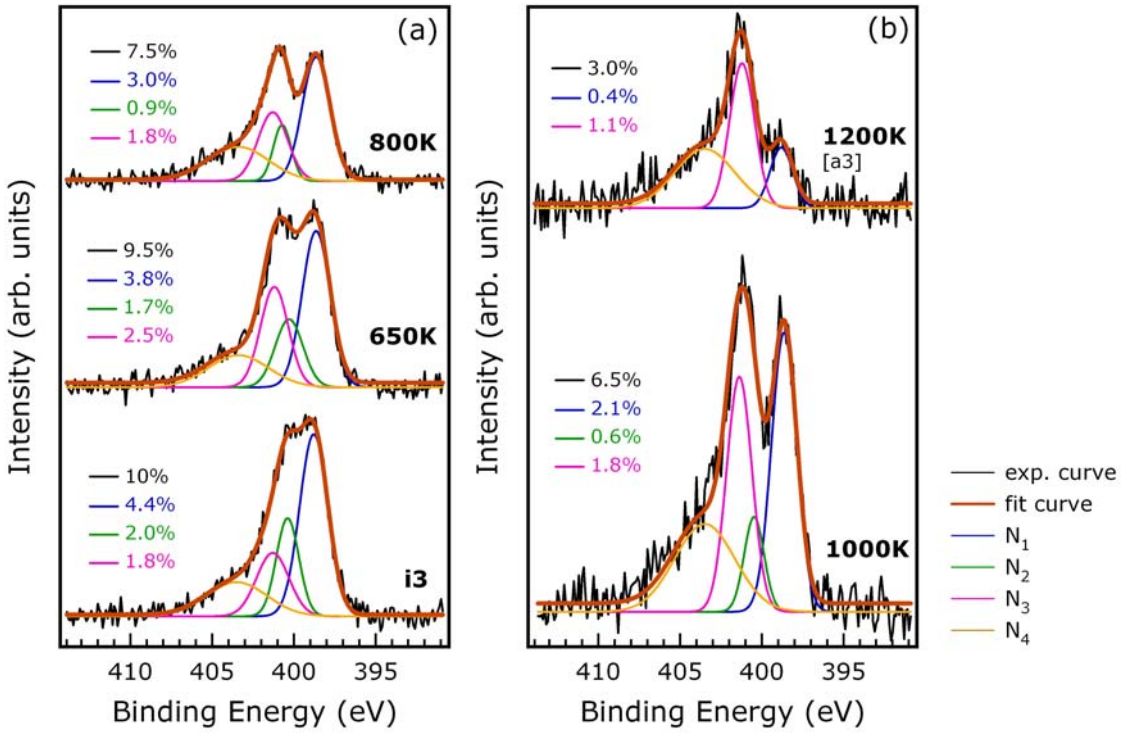

Fig. 5.6 – Gaussian multi-peak fitting of the N 1s core level spectra. All curves are normalized to the area of the corresponding C 1s core level spectrum. The total and the partial nitrogen atomic concentrations are reported next to each spectrum.

Further annealing at increasing temperatures produce at first the desorption of N_2 and then of N_3 atoms. Interestingly, about the 2% of substitutional atoms is stable up to 1000K, while the last step leads to the usual final state with nearly 1% of N_3 component. Finally, the trend of N_1, N_2, and N_3 atomic concentrations has been reported in fig. 5.7 versus increasing ion irradiation time and temperature. N_1 is the most sensitive component, being strongly reduced when temperatures higher than 800K have been reached, and the occurrence of a very stable bond involving substitutional nitrogen is pointed out.

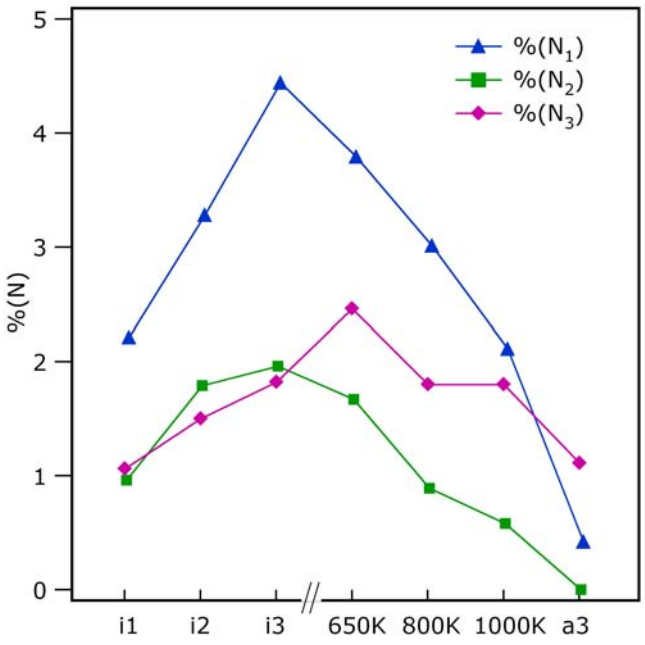

Fig. 5.7 – Trend of N_1, N_2, and N_3 atomic concentrations versus increasing amounts of implanted nitrogen and subsequent thermal treatment

5.5 Electronic properties: EELS and UPS measurements

We have observed significant changes also in EEL spectra, which have been reported in fig. 5.8 normalized to the elastic peak intensity. The intensity of the 6 eV loss peak, related to the $\pi \rightarrow \pi^*$ interband transitions, is drastically reduced in the i1 spectrum and is completely removed for higher doses of implanted nitrogen. This is the result of the remarkable modifications induced in the nanotube atomic structure, which is gradually and partially restored upon annealing up to 1200 K. Moreover, a feature located around 2 eV can be clearly identified on i2 and i3 curves; this peak does not vanish upon annealing, and might be caused by the presence of nitrogen atoms, but it is likely an effect of irradiation-induced damages.

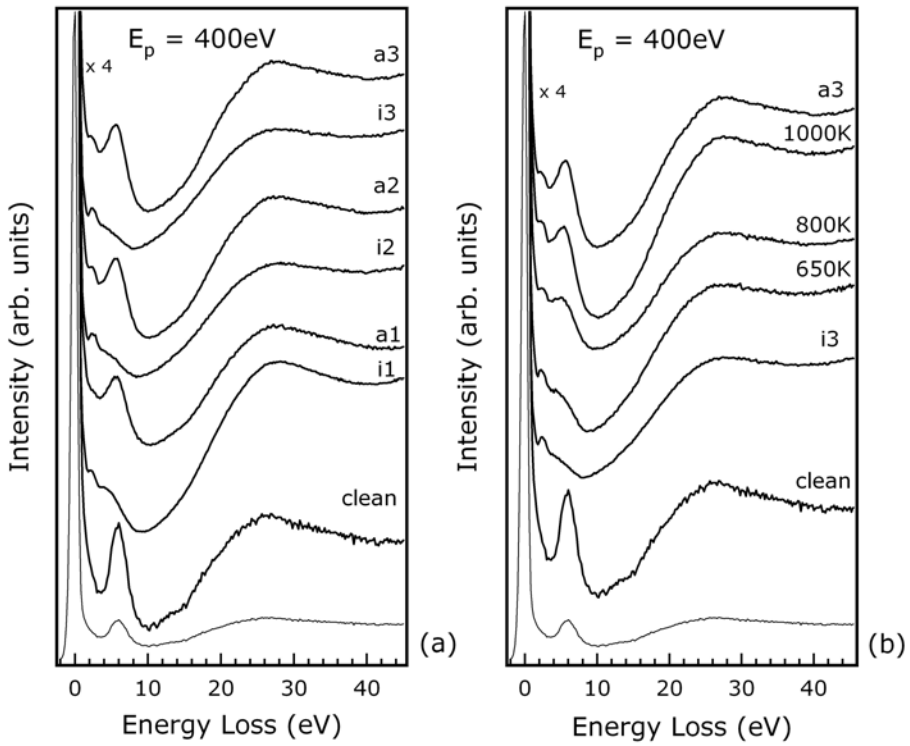

Fig. 5.8 – EEL spectra multiplied by 4 and vertically shifted acquired after (a) N_2^+ implantations (i1,i2,i3) and annealing at 1200K (a1,a2,a3), and (b) each annealing step following i3. The clean spectrum is shown as reference (bottom curve).

We have acquired further EEL spectra at higher resolution to monitor vHs-related features. Since ion implantation produces remarkable alterations of the CNT structure, we expected to observe the vanishing of loss peaks at 0.7 eV and 1.3 eV, which has indeed occurred just after short irradiation time. Moreover, even after reaching high temperatures, loss peaks connected to vHs interband transitions are washed out (see a1 and a2 curves of fig. 5.9). This behavior could be explained considering that the strong modifications suffered by the nanotube network are not completely recovered after thermal treatments. Moreover, we must take into account that the presence of substitutional nitrogen atoms, which do not desorb upon annealing at 1200K, might affect the electronic properties of the sample, resulting in the flat EEL spectra of fig. 5.9.

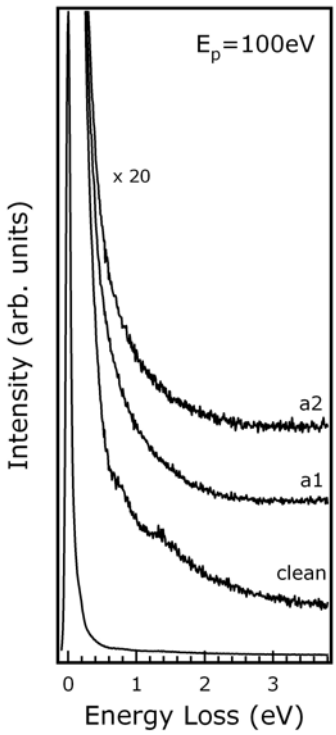

Fig. 5.9 – EEL spectra in the loss range (0÷4) eV

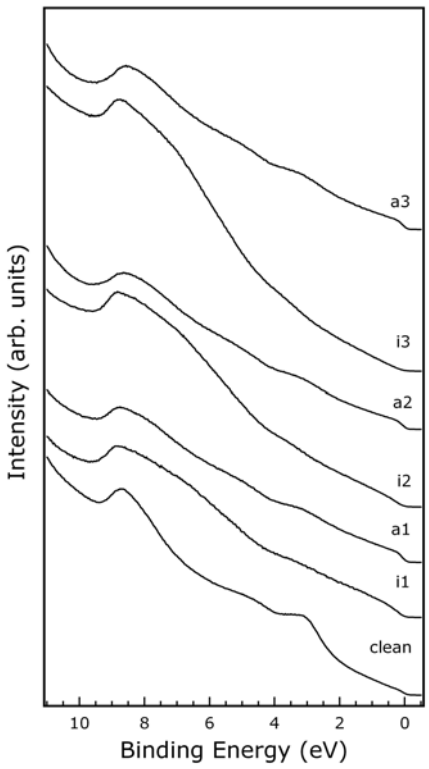

Fig. 5.10 – Valence band spectra acquired after N_2^+ implantations at increasing doses (i1,i2,i3) and annealing at 1200K (a1,a2,a3). The clean spectrum is shown as reference (bottom curve)

UPS measurements reveal that, similarly to EEL spectra, modifications of valence band properties (fig. 5.10) occur mainly in the π region. The π-band intensity undergoes a drastic reduction upon irradiation and is partially restored after annealing at 1200K, as can be better observed in the enlargements showed in fig. 5.11 (a) and (c). It is worth noting, moreover, that the disappearing of the π feature upon N-doping prevents us from detecting Fermi level shifts.

A further enlargement of the low-binding energy region (fig. 5.11(b)-(d)) highlights the great sensitivity of the spectral intensity around the Fermi level, which reveals the alterations suffered by the DOS. Since semiconducting tubes have zero DOS in an energy range centered on E_F and corresponding to the gap width, the small signal at E_F must be ascribed only to metallic tubes. If we focus on i1, i2 and i3 curves of fig. 5.11(b), we can see that two different slopes near E_F can be distinguished: at $E_B = 0$ (dashed line in fig. 5.11(b)) a metallic residual occurs, while a new steeper contribution arises at binding energies just below the Fermi level. Orange lines in fig. 5.11(b) represent linear fit curves of the flat section above E_F and of the steeper slope mentioned before. We have established that the crossing point of these fit-lines is about E_B=0 for i1 curve, and that it gradually shifts toward slightly higher binding energy (up to roughly 60 meV) as nitrogen dose increases. The energy resolution of UPS measurements does not allow us to do reliable quantitative analysis, nevertheless this trend suggests that N impurities induce a decrease of the DOS and give rise to a semiconducting-like behavior, due to both sp^3-coordinated N atoms and unsaturated sp^3 defective structures induced by implantation. This scenery is consistent with XPS measurements, according to which after ion irradiation the main contribution in N 1s core level spectra is caused by atoms arranged in diamond-like sp^3 configuration (see fig. 5.7), and it is well known that systems in which sp^3 hybridization occurs show insulating behavior. Moreover, the crossing point of the fit lines shifts backward just after the first annealing (T=650K), when a partial desorption of sp^3-N atoms has occurred.

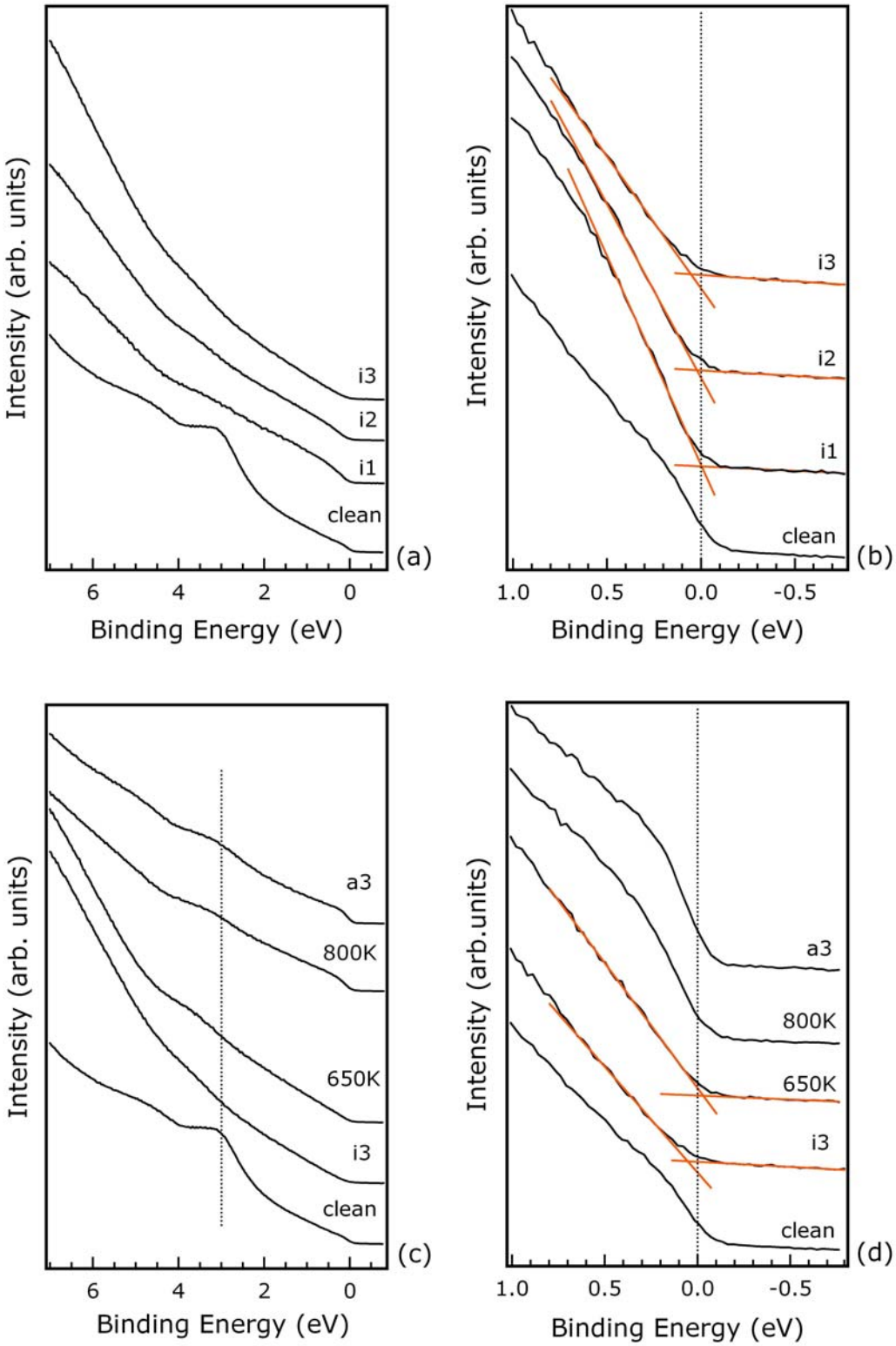

Fig. 5.11 – Valence band spectra of clean and N-implanted and annealed SWCNT bundles in the B.E. range (a)-(c) (-1÷7)eV, and (b)-(d) (-0.8÷1)eV

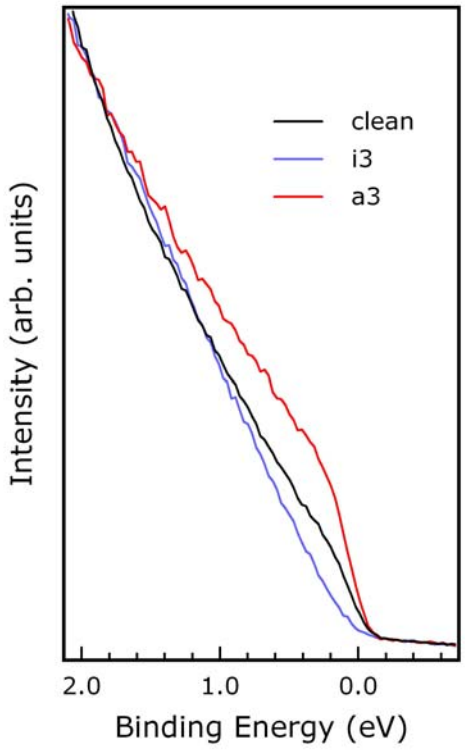

Fig. 5.12 – A comparison among valence band spectra of the clean, N-doped (highest dose) and annealed (1200K) sample, evidencing the modification suffered by the DOS profile near the Fermi level

A first evaluation of the temperature-induced effects can be carried out from a comparison of the curves reported in fig. 5.11(d): the spectral intensity at the Fermi level undergoes progressive enhancement upon annealing at increasing temperatures. The remarkable increase of DOS near E_F can be better evaluated looking at fig. 5.12, as only the clean, i3 and a3 curves have been reported without vertical offset (a similar behavior is observed for i1, a1 and i2, a2). This result is very interesting, because it can be regarded as an effect induced by only substitutional nitrogen, as we have already seen that only this configuration is present after the annealing at 1200K. The DOS enhancement at the Fermi level is therefore a striking effect of the charge transfer produced by sp^2-hybridized nitrogen substituting carbon atoms.

5.6 Conclusions

A comprehensive study on both chemical and electronic properties of N-implanted SWCNT bundles [108] has provided us with a quite clear picture of the doping-induced effects on the nanotube network. After being accelerated toward the sample, N_2^+ ions break up, and highly energetic nitrogen atoms penetrate into the sample; ion irradiation produces defects and structural disorder, and strongly affects the 2p-π band structure. As for chemical properties, three possible configurations for N-C bond can be distinguished. Nitrogen atoms can interact with sp^3-hybridized C in a tetrahedral configuration or take the place of carbon atoms. In the last case, N can form an sp^2 bond with three carbon neighbors (substitutional doping) in a graphite-like arrangement, or with two carbon atoms in a defective pyridine-like structure. The total N atomic concentration is almost unaffected by heating at 650K, that however partially restores the CNT structure. Higher temperature (1200K) annealing induces the desorption of nitrogen placed in both tetrahedral an defective sites, while about 1% of substitutional nitrogen impurities still remains on the sample. Moreover, we have detected a noteworthy enhancement of the density of states near the Fermi level, which accounts for the charge transfer due to substitutional doping. Hence, according to our results, nitrogen ion implantation seems to be a promising technique to carry out CNT doping. Furthermore, this preliminary study suggests the opportunity of searching for the optimal value of beam energy, in order to reduce structural damages and maximize the concentration of substitutional impurities.

Chapter 6

Synthesis of multi-wall carbon nanotubes

6.1 Introduction

Three methods are commonly employed for the growth of both multi-wall and single-wall CNTs: arc-discharge, laser ablation and chemical vapor deposition (CVD) [109]. In the first method, CNTs are grown through the arc-vaporization of two graphite electrodes placed in a chamber filled with an inert gas (Ar, He) at low pressure (≈500 mbar). The high-temperature discharge, which is generated through a dc current of 50-120 A driven by nearly 20-25 V, causes a gradual reduction of the anode length, while a rod-shaped deposit forms on the cathode. The quantity and purity of CNTs depends on several parameters, such as gas pressure and discharge current. Pure graphite electrodes are used for MWCNTs production [110]: the nanotubes, arranged in bundles, are found in the inner region of the cathode deposit, where the temperature reaches its maximum value (3000 K). In addition to MWCNTs, nanoparticles, fullerenes, and amorphous carbon are produced; however, advanced methods have been developed in order to get high-purity MWCNT samples without performing the purification processes, which may damage the tube structure [111,112]. The use of catalysts (e.g. Co, Ni, Fe, Y, or

mixtures Fe/Ni, Co/Ni) is necessary to synthesize SWCNTs [5], with diameters ranging from 1.2 nm to 1.5 nm, but has the inconvenience that large amounts of catalysts are still present in the produced soot. Hence, several purification procedures, e.g. oxidation or acid treatment, are carried out in order to take apart nanotubes from impurities [109].

The CNT synthesis can be achieved also through laser ablation technique [114,115]: a graphite target, placed in an oven at 1400 K filled with inert gas, is vaporized through a high-power laser source (pulsed or continuous). Also in this case MWCNTs are produced if a pure graphite target is employed, while the presence of catalytic particles is required to synthesize SWCNTs, which usually aggregate in ropes. Laser ablation produces smaller amounts of CNTs with respect to arc-discharge method, but with a better degree of purity.

In the CVD method [116] a catalyst is heated to high temperatures (700-1200 K) in a tube furnace, while flowing a hydrocarbon gas (e.g. CH_4, C_6H_6) through the tube reactor. In this process, the dissociation of hydrocarbon molecules is catalyzed by transition metal nanoparticles (Fe, Co, Ni) stuck on a porous material as alumina. At high temperatures carbon is soluble in these metals, and the dissolution and saturation of carbon atoms in the nanoparticles is followed by precipitation of carbon and the formation of tubular sp^2 structures. CVD offers some advantages for large-scale synthesis, since it allows continuous production of both MWCNTs and SWCNTs; moreover, ordered nanotube structures can also be realized, achieving a defined tube alignment, while only random distributions of nanotubes can be produced with arc-discharge technique.

In this chapter we will present some interesting findings related to the synthesis of MWCNTs, carried out by arc-discharge method, which have been analyzed both through Scanning Electron Microscopy (SEM) and Raman spectroscopy.

6.2 MWCNT synthesis by arc-discharge method

The synthesis of MWCNTs by arc-discharge technique has been carried out employing two graphite electrodes (cathode and anode diameter of 10 mm and 3 mm, respectively) mounted in a chamber which was previously evacuated, and subsequently filled with high purity helium gas at 500 mbar pressure. A scheme of the system is reported below in fig. 6.1.

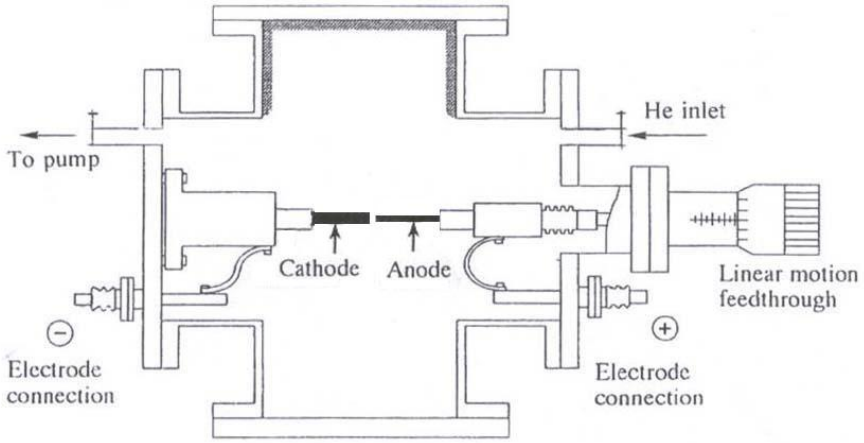

Fig. 6.1 – Cross section of a system for CNT arc-discharge synthesis

The high-temperature discharge has been created using a current of 60 A driven by about 25 V across the electrodes. During the discharge, the cathode was kept at a temperature of nearly 350 K, through a liquid nitrogen-based cooling system; the temperature has been indirectly measured by a thermocouple fixed to the end of the copper-made cathode support, next to the graphite rod. Moreover, the discharge current has been controlled manually by keeping the cathode-anode distance constant (roughly 1mm), as the anode could be translated along its axis. Two sets of samples have been produced, which will referred to as S1 and S2 hereafter; in the first set, pure graphite electrodes have been employed. For the second, a catalytic mixture (Ni-Cr, in the weight proportion 8:2) has been inserted in a hole (d=1 mm) made in the center of the anode. In fig. 6.1(a) and (b) two

images of the electrodes, taken before and after the discharge, have been reported. A discharge lasting approximately 100 s resulted in the formation of a small rod-shaped deposit on the cathode, shown in the inset of fig. 6.1(b).

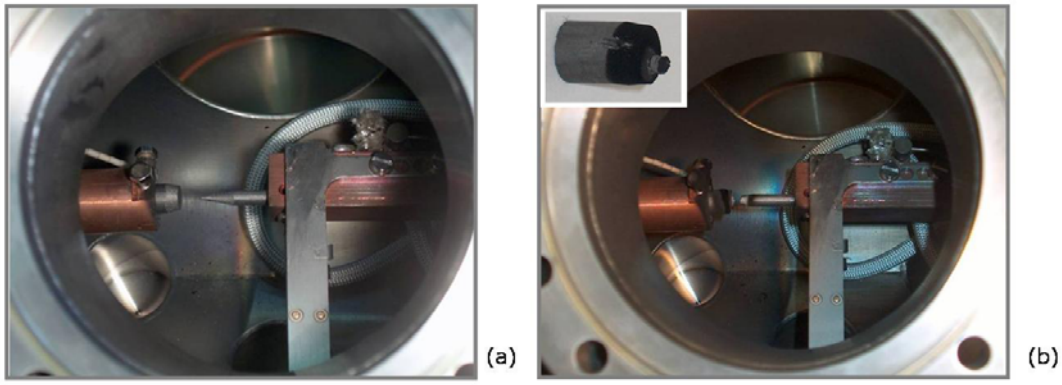

Fig. 6.2 – The graphite electrodes (a) before, and (b) after the discharge. In the inset of panel (b) the deposit on the cathode is shown

6.3 SEM and Raman techniques

The deposited cathodes have been analyzed first by SEM, which gives topographical images of a sample resulting from differences of the local secondary electron emissivity [79]. SEM images have been acquired using a Stereoscan 360 microscope by Cambridge Instruments, equipped with an X-ray microanalysis system.

Then, both spatial- and temperature-dependent Raman investigation has been carried out. Raman spectroscopy is a powerful technique which exploits the Raman effect: when a photon beam is incident on a molecule, most photons undergo elastic scattering. However, a small fraction is inelastically scattered at frequencies which can be lower (Stokes scattering) or even higher (anti-Stokes) than the primary frequency [13]. The Raman shifts, measured with respect to the elastic frequency, correspond to vibrational modes of the analyzed sample. The anti-Stokes spectrum is always weaker than the Stokes one, and the ratio of anti-Stokes to

Stokes intensity, corresponding to a vibrational frequency ω, provides a measure of temperature since $I_{Stokes} / I_{Antistokes} \propto \exp(-\hbar\omega / kT)$. It is worth noting that only vibrational modes which satisfy the Raman selection rules can be detected. As regards CNTs, Raman spectroscopy is widely employed, since it is a readily available technique which provides several information on their structural and physical properties without damaging the samples [11]. CNT spectra are characterized by two graphite-related Raman-active modes, the D and the G bands, located in the ranges (1300-1350) cm^{-1} and (1550-1600) cm^{-1}, respectively. The D band intensity is directly proportional to the number of structural defects, while the G band corresponds to a tangential vibration of carbon atoms, deriving from a graphene in-plane optical mode. Moreover, the center of diameter distribution of a bundle or the diameter of a single tube can be estimated from the frequency of the radial breathing mode (RBM), which is detected at about 200 cm^{-1} and depends on the tube diameter according to the relation

$$\omega_{\mathrm{RBM}} = \frac{284}{d(\mathrm{nm})}\,\mathrm{cm}^{-1} \tag{6.1}$$

Moreover, the occurrence of vHs with very large DOS allows the collection of Raman spectra even from a single SWCNT [117]. In fact, resonant effects occur if the incident or scattered photon energy matches that of an electronic transition involving vHs, and the strong electron-phonon coupling causes a remarkable enhancement of Raman signal intensity. Finally, it is also possible to gain information on the spectral profile of the one-dimensional joint DOS near a vHs.

Raman measurements, with a spectral resolution of 1-2 cm^{-1}, have been performed using a microprobe set-up (ISA-Jobin-Yvon, model Labram) equipped with a CCD detector and a He-Ne laser (632.8 nm emission). A special X-Y stage for spectral mapping was used to carry out spatial-dependent analysis; furthermore, different temperatures of the sample have been achieved using several optical density (O.D.) filters, through which the irradiance could be varied with respect to the value attained with the unfiltered laser beam (about 50 kW/cm^2).

6.4 SEM analysis

In the SEM image of the cathode S1, reported in fig. 6.3(a), we notice the occurrence of a symmetrical structure: a white corona, corresponding to a region with enhanced secondary electron emission, draws up the boundaries of the smooth deposited surface. The corona extends for almost all the circumference of the flat zone, separating it from the outer, coarse grained, region of the cathode, which is made of graphite-like carbon conglomerate (see enlargement of the border in fig. 6.3(b)). An image at higher magnification of the inner area reveals the presence of filaments on a nanoscopic scale, with diameters compatible with those of MWCNTs (fig. 6.3(c)).

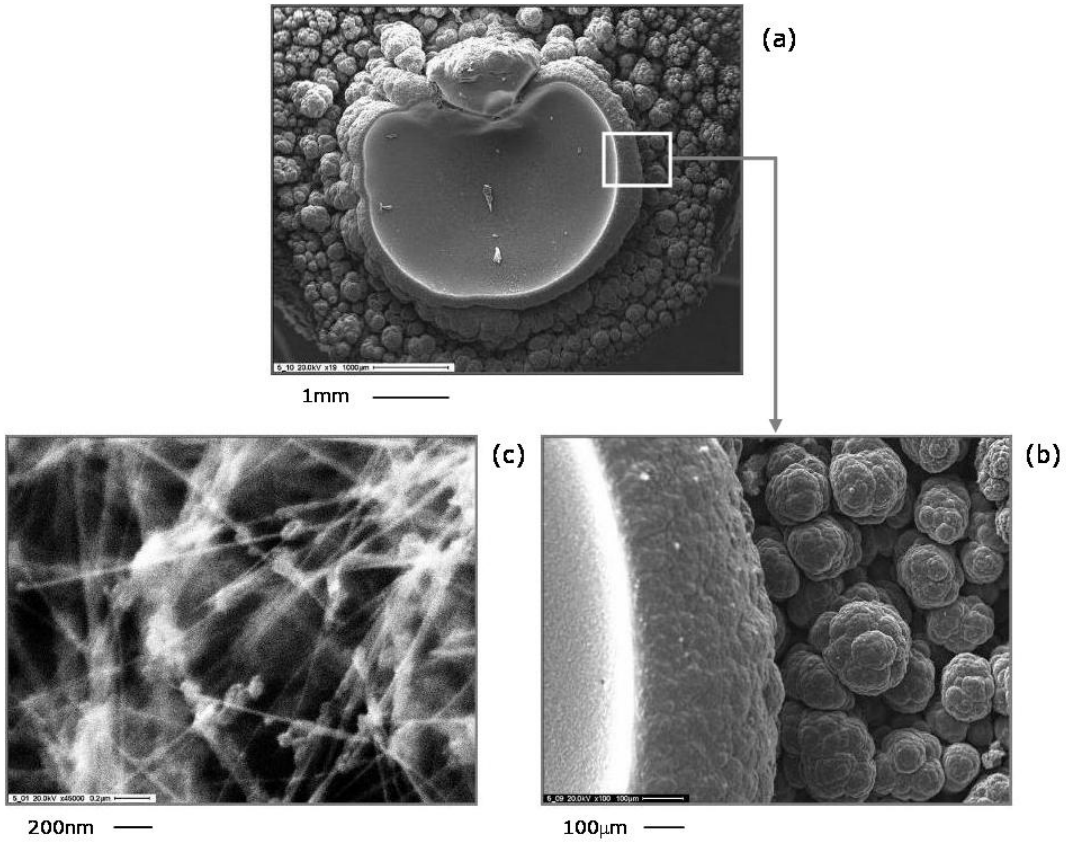

Fig. 6.3 – SEM images: (a) deposit on cathode S1 (pure graphite electrode); (b) an enlargement of the border region; (c) high magnification of the smooth region inside the corona, revealing the presence of tubular structures

The structure of cathode S2 is instead much less regular: the white corona is partially present along the circumference, and some "hills" break the uniformity of the inner smooth zone. Nevertheless, also in this case tubular structures with different diameters occur in the central region, as shown in the image with the best magnification (fig. 6.4(c)).

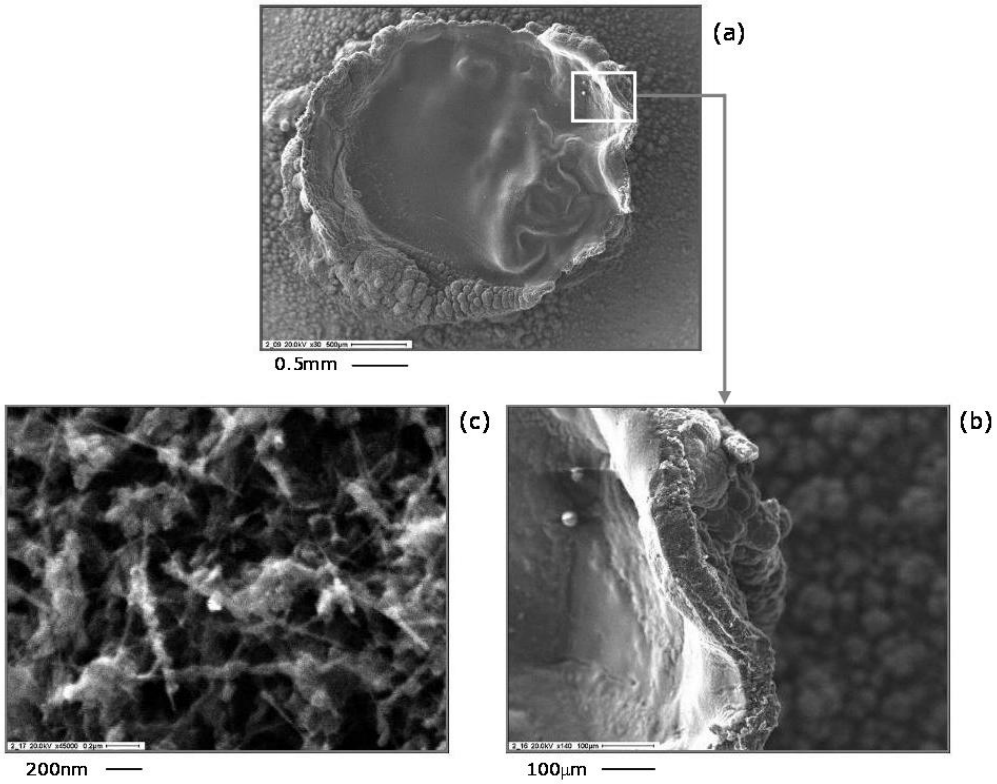

Fig. 6.4 – SEM images: (a) cathode S2 (graphite electrode with inserted catalytic mixture); (b) an enlargement of the border region; (c) high magnification of the inner region, evidencing the occurrence of tubular structures

6.5 Raman analysis

Several Raman spectra have been collected from both cathodes S1 (fig. 6.5) and S2 (fig. 6.6), moving radially from the deposit borders toward its center (see the inset of fig. 6.5). In fig. 6.5, the topmost curve corresponds to a spot located

on the external boundary of the white corona; for distances of (5-150) μm from the border, an unusual feature is detected besides the typical D and G bands (and the overtone of the D band, found approximately at 2700 cm^{-1}). This band, which will be labeled "L" hereafter, is located in the wave number range (1780-1860) cm^{-1}. The L/G intensity ratio is very low for distances from the border larger than 500 μm, and approximates zero at the center of the cathode.

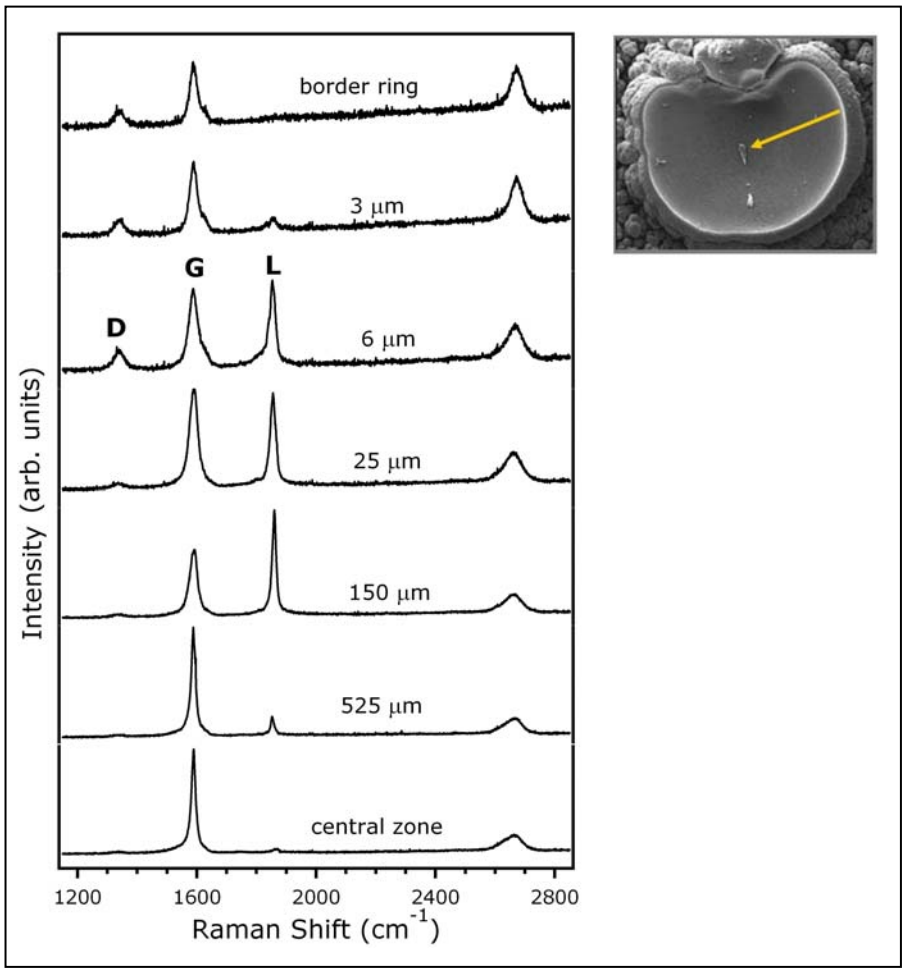

Fig. 6.5 – Raman spectra of the cathode S1 acquired on different spots, moving radially from the border ring (top curve) toward the center, as illustrated in the inset

The occurrence of this novel Raman band has been reported in some recent works [8,118,119], and it has been attributed to the vibrations of sp linear chains of

carbon atoms lying on the axis inside the MWCNTs. The first observation of an atomic wire located inside the inner tube of MWCNTs has been provided by a High Resolution Transmission Electron Microscopy (HRTEM) study [120], made on samples grown by arc discharge in helium atmosphere. The other results, concerning MWCNT obtained in hydrogen atmosphere at low pressure, are based on the observation of strong Raman bands at about 1850 cm^{-1} and are supported also by some TEM images [8]. The isolated molecules with pure sp-hybridization (carbynes) can present two different bond configurations: cumulene, with only double bonds (C=C=C=C=C), and polyyne, with alternating single-triple bonds (C≡C–C≡C–C). The former should exhibit metal-like conductivity, because of electrons occupying a half filled band; moreover, as all metallic one-dimensional systems, is unstable under the so-called Peierls distortion, which leads to the formation of a configuration characterized by a Bond Length Alternation (BLA) [121]. Moreover, the distorted molecule becomes insulating or semiconducting, because there are two atoms per unit cell. The vibrational frequencies of carbyne Raman active modes vary from 1800 cm^{-1} to 2200 cm^{-1}, depending on the chain length and the bond configuration. Raman bands in the range (1900-2200) cm^{-1} have been observed studying carbonaceous materials grown in an UHV cluster beam apparatus [122], and have been assigned to cumulenic and polyynic carbon chains. These systems are very fragile, with short lifetimes of the order of hours. Carbon chains enclosed in nanotubes are instead highly stable, in fact the Raman signal is detected even after annealing at 1800 K [123]. Furthermore, an extraordinary average length of the encapsulated chains, about 100 atoms, has been postulated to explain the great down-shift of vibrational frequency with respect to carbyne. These results suggest that the nanotube constitutes a protecting environment for these systems.

The topmost curve of fig. 6.5, collected from the outer ring zone of cathode S1, resembles a typical spectrum of disordered graphite more than MWCNT; moving toward the center, L band relative intensity grows and reaches the

maximum value in correspondence of a remarkable decrease of the intensity ratio D/G, usually assumed as index of disorder. Finally, L band intensity is negligible in the zones next to the center of the cathode, where we notice a very small D/G ratio, and a narrowing of the G band: this behavior indicates the presence of very homogeneous and pure MWCNTs. For the cathode S2, on the contrary, the intensity ratio D/G is always high (see fig. 6.6), even in the central zones, showing a minimum value in correspondence with the maximum intensity of L band.

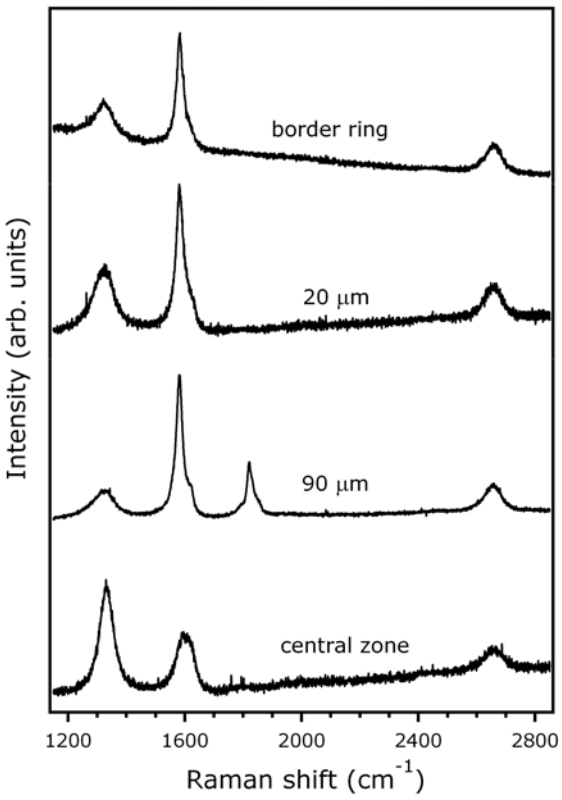

Fig. 6.6 – Raman spectra of the cathode S2 acquired moving radially from the border ring (top curve) toward the center

Our experimental results point out that the presence of the catalyses is not strictly related to the formation of linear carbon chains inside the nanotubes, while it strongly affects the quality of the host MWCNT. The occurrence of particular physical and chemical conditions might promote the formation of stable chains

inside the tubes at the white boundaries of the arc discharge plasma, as pointed out by a strong L band intensity in that region. Moreover, the plasma conditions at the cathode center favor the growth of pure, homogeneous and well aligned MWCNT. Summarizing, results obtained from spatial-dependent Raman spectra of different cathodes suggest that some degree of order is required for the formation of carbon chains inside the nanotubes, although this condition alone does not assure their occurrence. In fact, in the central region of cathode S1 we have detected a feasible L band intensity connected with a well-ordered MWCNT configuration. Furthermore, in different spots of the same cathode and for different cathodes significant modifications of the frequency values, bandwidths and intensity ratio between peaks occur.

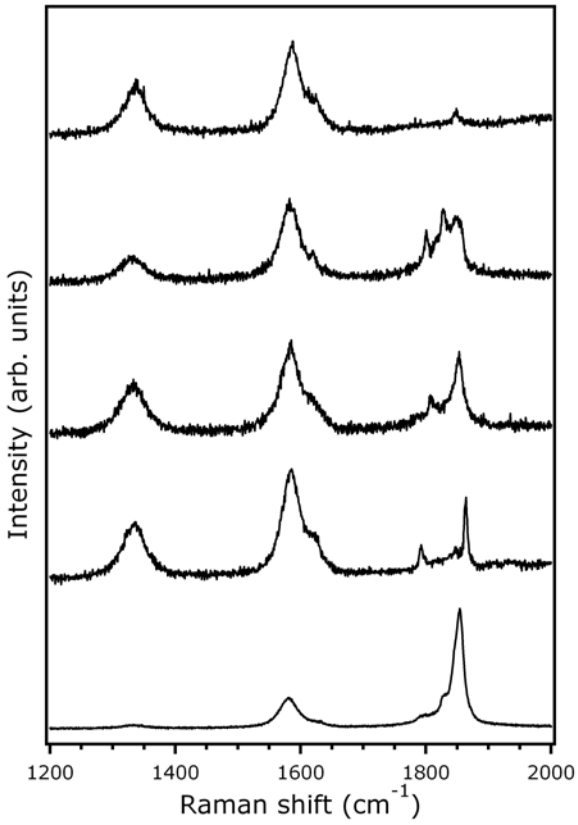

Fig. 6.7 – Raman spectra of the cathode S1 acquired on different spots, showing the significant variability of the L band fine structure

The L band exhibits a fine structure, and three sub-bands are generally observed in the ranges (1850-1860) cm^{-1}, (1820-1830) cm^{-1}, and (1780-1800) cm^{-1}. The band width value is approximately 20 cm^{-1}, but sometimes very narrow peaks (≈6 cm^{-1} band width) can be observed. These results can be interpreted taking into account some theoretical studies concerning the properties of chains inserted in host tubes [124-126]. It is worth noting that these theoretical works consider as outer envelope a SWCNT, while experimental evidences of inner carbon chains regard mainly MWCNT, and only recently the formation for high temperature of inner carbon chain in double walled nanotubes has been reported [125]. According to theoretical calculations [121], chain-tube interactions, due to charge transfer and hybridization, can partially suppress the BLA resulting from Peierls instability. This effect depends on the interaction strength, which in turn is related to the host nanotube chirality. Hence, the observed L band fine structure can be explained as an effect of modulation of the carbon chain stretching frequency due to the occurrence of host MWCNTs with different chiralities. Very narrow L peaks, which are rarely observed, might correspond to a high local homogeneity of MWCNT chirality and inner chain length.

Finally, the temperature dependence of the L bands has been investigated, choosing spots associated to a good L band signal at room temperature. Raman spectra collected from cathode S1 are reported in fig. 6.8, where we notice that the L band intensity strongly decreases with respect to the G band as temperature increases. The observed evolution of L bands can be interpreted within a picture of a reversible thermally-driven phase transition, involving a decrease of the BLA related to the Peierls distortion. The high temperature can indeed modify the equilibrium of the chain-tube interactions and produce a strong reduction of BLA, resulting in a transition from a Raman-active polyynic chain, with localized electron wave functions, toward a non Raman-active [125] cumulenic chain, with delocalized electronic distribution and metal-like conductivity.

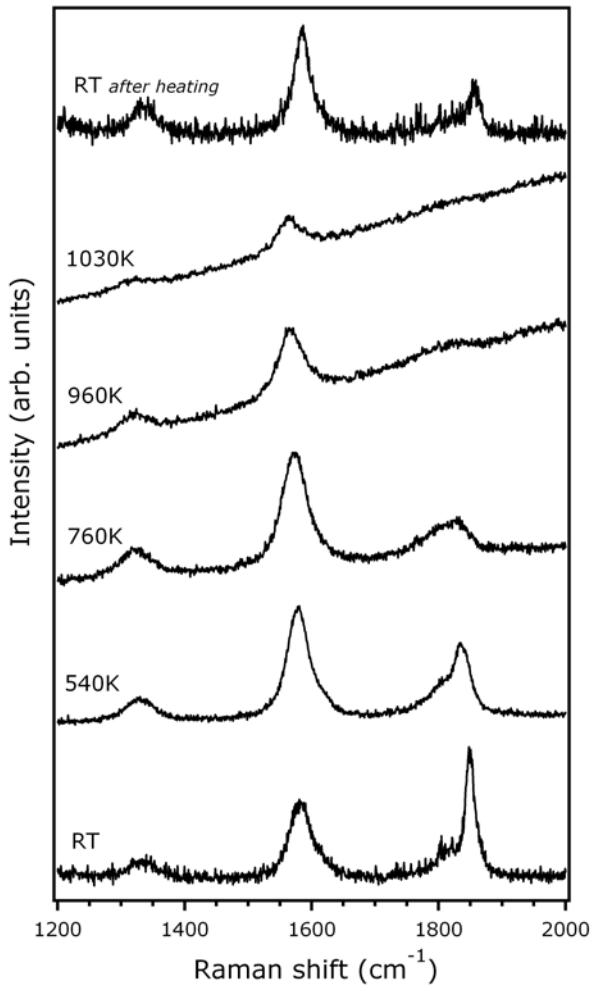

Fig. 6.8 – Raman spectra of the cathode S1 as a function of temperature; the topmost curve has been acquired after cooling down again the sample

Furthermore, the intensity of chain Raman mode, which suffers a strong reduction upon annealing, is partially recovered (see topmost curve of fig. 6.8) when the sample is brought back to room temperature. Our findings constitute the first evidence of a reversible temperature-related phase transition involving carbon chains encapsulated in MWCNTs.

6.6 Conclusions

Raman measurements, performed on MWCNTs grown by arc discharge method in He atmosphere, have pointed out the occurrence of a band at 1780-1860 cm^{-1}, regardless of the use of a catalytic Ni-Cr alloy in the synthesis process [127]. This band has been attributed to the presence of carbon linear chains inside the innermost tube. The maximum Raman signal from the chain-related L bands is found inside a circular region, in correspondence with enhanced secondary electron emission, as evidenced by a strong white color in the SEM images. Furthermore, a temperature-dependent Raman study, up to about 1000K, has revealed for the first time a phase transition trend [128], which seems to be related to a strong, reversible reduction of the Peierls distortion at high temperatures.

Conclusions

We have presented and discussed the results of a spectroscopic study concerning the effects induced on the electronic and chemical properties of SWCNT bundles by the insertion of electron donor species. We have pointed out that different aspects can be investigated through doping with nitrogen atoms and alkali metals. Nitrogen implantation has revealed to be a promising technique to achieve significant amounts of substitutional impurities; nitrogen realises a much more effective doping than alkali metals, since small atomic concentrations lead to stronger modifications of electronic properties. For this reason, nitrogen doping might be a suitable method in order to improve performance of nanotubes for industrial applications. As regards lithium intercalation, we have observed modifications suffered by the valence band states and the van Hove singularities, which are features representative of the one-dimensional nature of nanotubes. Our results have revealed the occurrence of cross-links among tubes mediated by Li-C covalent-like bond. Hence, this investigation has provided interesting information regarding a widely studied topic, which concerns the electronic properties of one-dimensional systems. Finally, through the analysis of CNTs synthesized by arc-

discharge method, we have found out the occurrence of MWCNTs encapsulating carbon linear chains, which are also sensitive to thermal treatments. It is worth noting that the existence of these novel systems has been recently discovered by accident on the cathode deposit of a standard apparatus for arc-discharge nanotube growth, just as the studies on fullerene synthesis were the occasion of the discovery of carbon nanotubes. Hence, carbon-based systems still keep on offering new attractive challenges for fundamental and technological research.

References

[1] S. Iijima, *Nature* 354, 56 (1991)

[2] R.-H. Xie, J. Zhao, and Q. Rao, *Encyclopedia of Nanoscience and Nanotechnology* X, 1 (2004)

[3] G. Zhang, W. Duan, and B. Gu, *Appl. Phys. Lett.* 80, 2589 (2002)

[4] H. Rauf, T. Pichler, M. Knupfer, J. Fink, and H. Kataura, *Phys. Rev. Lett.* 93, 096805 (2004)

[5] R. Larciprete, L. Petaccia, S. Lizzit, and A. Goldoni, *Phys. Rev. B* 71, 115435 (2005)

[6] R. Droppa Jr., C.T.M. Ribeiro, A.R. Zanatta, M.C. dos Santos, and F. Alvarez, *Phys. Rev. B* 69, 045405 (2004)

[7] J. Kotakoski, A.V. Krasheninnikov, Y. Ma, A.S. Foster, K. Nordlund, and R.M Nieminen, *Phys. Rev. B* 71, 205408 (2005)

[8] X. Zhao, Y. Ando, Y. Liu, M. Jinno, and T. Suzuki, *Phys. Rev. Lett.* 90, 187401 (2003)

[9] H.W. Kroto, J.R. Heath, S.C. O'Brien, R.F. Curl, and R.E. Smalley, *Nature* 318, 162 (1985)

[10] S. Iijima and T. Ichiashi, *Nature* 363, 603 (1993)

[11] R. Saito, G. Dresselhaus, M.S. Dresselhaus, "*Physical Properties of Carbon Nanotubes*", Imperial College Press, London (1998)

[12] N. Hamada, S.-i. Sawada, and A. Oshiyama, *Phys. Rev. Lett.* 68, 1579 (1992)

[13] S. Reich, C. Thomsen, and J. Maultzsch, "*Carbon Nanotubes*", Wiley-Vch (2004)

[14] J. W. Mintmire and C. T. White, *Phys. Rev. Lett.* 81, 2506 (1998)

[15] Ph. Lambin, *C. R. Physique.* 4, 1009 (2003)

[16] J.W.G. Wildöer, L.C. Venema, A.G. Rinzler, R.E. Smalley, and C. Dekker, *Nature* 391, 59 (1998)

[17] T. W. Odom, J.-L. Huang, P. Kim, and C. M. Lieber, *Nature* 391, 62 (1998)

[18] L.C. Venema, J.W. Janssen, M. R. Buitelaar, J.W.G. Wildöer, S.G. Lemay et al., *Phys. Rev. B* 62, 5238 (2000)

[19] A. Jorio, A.G.S. Filho, G. Dresselhaus, M.S. Dresselhaus, R. Saito et al., *Phys. Rev. B* 63, 245416 (2001)

[20] M.J. O'Connel, S.M. Bachilo, C.B. Huffman, V.C. Moore, M.S. Strano et al., *Science* 297, 593 (2002)

[21] M. Ouyang, J.-L. Huang, C.L. Cheung, and C.M. Lieber, *Science* 292, 702 (2001)

[22] A.A. Maarouf, C.L. Kane, and J.L Mele, *Phys. Rev. B* 61, 11156 (2000)

[23] H. Ishii, H. Kataura, H. Shiozawa, H. Yoshioka, H. Otsubo et al., *Nature* 426, 540 (2003)

[24] C. Hartwigsen, W. Witschel, and E. Spohr, *Phys. Rev. B* 64, 085420 (2001)

[25] L. Duclaux, *Carbon* 40, 1751 (2002)

[26] R.S. Lee, H.J. Kim, J.E. Fischer, J. Lefebvre, M. Radosavljević, et al., *Phys. Rev. B* 61, 4526 (2000)

[27] R.S. Lee, H.J. Kim, J.E. Fischer, A. Thess, and R.E. Smalley, *Nature* 388, 255 (1997)

[28] A.M. Rao, P.C. Eklund, S. Bandow, A. Thess, and R.E. Smalley, *Nature* 388, 257 (1997)

[29] S. Suzuki, C. Bower, Y. Watanabe, and O. Zhou, *Appl. Phys. Lett.* 76, 4007 (2000)

[30] J. Zhao, J. Han, and J.P. Lu, *Phys. Rev. B* 65, 193401 (2002)

[31] S. Suzuki, C. Bower, and O. Zhou, *Chem. Phys. Lett.* 285, 230 (1998)

[32] X. Liu, T. Pichler, M. Knupfer, and J. Fink, *Phys. Rev. B* 67, 125403 (2003)

[33] P. Dubot and P. Cenedese, *Phys. Rev. B* 63, 241402 (2001)

[34] P. Chen, *Science* 285, 91 (1999)

[35] A.C. Dillon, K.M. Jones, T.A. Bekkedahl, C.H. Kiang, D.S. Bethune, and M.J. Heben, *Nature* 386, 377 (1997)

[36] Y. Ye, C.C. Ahn, C. Witham, B. Fultz, J. Liu et al, *Appl. Phys. Lett.* 74, 2307 (1999)

[37] R.T. Yang, *Carbon* 38, 623 (2000)

[38] F.E. Pinkerton, B.G. Wicke, C.H. Olk, G.G. Tibbets, G.P. Meisner et al., *J. Phys. Chem. B* 104, 9460 (2000)

[39] E.-C. Lee, Y.-S.Kim, Y.-G. Jin, and K.J. Chang, *Phys. Rev. B* 66, 073415 (2002)

[40] K. Shen, H. Xu, Y. Jiang, and T. Pietraß, *Carbon* 42, 2315 (2004)

[41] Z.H. Zhu, G.Q. Lu, and S.C. Smith, *Carbon* 42, 2509 (2004)

[42] H. Shimoda, B. Gao, X.P. Tang, A. Kleinhammes, L. Fleming et al., *Phys. Rev. Lett.* 88, 015502 (2002)

[43] J. Zhao, A. Buldum, J. Han, and J.P. Lu, *Phys. Rev. Lett.* 85, 1706 (2000)

[44] V. Meunnier, J. Kephart, C. Roland, and J. Bernholc, *Phys. Rev. Lett.* 88, 075506 (2002)

[45] S.J. Tans, M.H. Devoret, H. Dai, A. Thess, R.E. Smalley et al., *Nature* 386, 474 (1997)

[46] R. Egger and A.O. Gogolin, *Phys. Rev. Lett.* 79, 5082 (1997)

[47] C. Kane, L. Balents, and M.P.A. Fischer, *Phys. Rev. Lett.* 79, 5086 (1997)

[48] S.J. Tans, M.H. Devoret, R.J.A. Groeneveld, and C. Dekker, *Nature* 394, 761 (1998)

[49] M. Bockrath, D.H. Cobden, P.L. McEuen, N.G. Chopra, A. Zettl, et al., *Science* 275, 1922 (1997)

[50] M. Bockrath, D.H. Cobden, J. Lu, A.G. Rinzler, R.E. Smalley et al., *Nature* 397, 598 (1999)

[51] J. Kong, N.R. Franklin, C. Zhou, M.G. Chapline, S. Peng et al., *Science* 287, 622 (2000)

[52] P.G. Collins, K. Bradley, M. Ishigami, and A. Zettl, *Science* 287, 1801 (2000)

[53] G.U. Sumanasekera, C.K.W. Adu, S. Fang, and P.C. Eklund, *Phys. Rev. Lett.* 85, 1096 (2000)

[54] J. Zhao, A. Buldum, J. Han, and J.P. Lu, *Nanotechnology* 13, 195 (2002)

[55] S. H. Jhi, S.G. Louie, and M.L. Cohen, *Phys. Rev. Lett.* 85, 1710 (2000)

[56] D. Kang, N. Park, J.-h. Ko, E. Bar, and W. Park, *Nanotechnology* 16, 1048 (2005)

[57] D.C. Sorescu, K.D. Jordan, and Ph. Avouris, *J. Phys. Chem B*, 105, 11227 (2001)

[58] H. Ulbricht, G. Moos, and T. Hertel, *Phys. Rev. B* 66, 075404 (2002)

[59] D. Lamoen and B.N. Persson, *J. Chem. Phys.* 108, 3332 (1998)

[60] S. Dag, O. Gülseren, T. Yildirim, and S. Ciraci, *Phys. Rev. B* 67, 165424 (2003)

[61] P. Giannozzi, R. Car, and G. Scoles, *J. Chem. Phys.* 118, 1003 (2003)

[62] A. Tchernatinsky, S. Desai, G.U. Sumanasekera, C.S. Jayanthi, S.Y. Wu et al., *J. Appl. Phys.* 99, 034306 (2006)

[63] A. Goldoni, R. Larciprete, L. Petaccia, and S. Lizzit, *J. Am. Chem. Soc.* 125, 11329 (2003)

[64] R. Larciprete, A. Goldoni, and S. Lizzit, *Nucl. Instr. and Meth. in Phys. Res. B* 200, 5 (2003)

[65] A. Goldoni, L. Petaccia, L. Gregoratti, B. Kaulich, A. Barinov et al., *Carbon* 42, 2099 (2004)

[66] M. Monthioux, B.W. Smith, B. Burteaux, A. Claye, J.E. Fischer, and D.E. Luzzi, *Carbon* 39, 1251 (2001)

[67] A.H. Nevidomskyy, G. Csányi, and M.C. Payne, *Phys. Rev. Lett.* 91, 105502 (2003)

[68] Y. Miyamoto, M.L. Cohen, and S.G. Louie, *Solid State Commun.* 102, 605 (1997)

[69] X. Ma and E.G. Wang, *Appl. Phys. Lett.* 78, 978 (2001)

[70] S.H. Lim, H.I. Elim, X.Y. Gao, A.T.S. Wee, W. Ji et al., *Phys. Rev.* 73, 045402 (2006)

[71] H.C. Choi, S.Y. Bae, J. Park, K. Seo, C. Kim et al., *Appl. Phys. Lett.* 85, 5742 (2004)

[72] J.W. Jang, C.E. Lee, S.C. Lyu, T.J. Lee, C.J. Lee et al., *Appl. Phys. Lett.* 84, 2877 (2004)

[73] J. Kotakoski, J.A.V. Pomoell, A.V. Krasheninnikov, and K. Nordlund, *Nucl. Instr. and Meth. in Phys. Res. B* 228, 31 (2005)

[74] D. Srivastava, M. Menon, C. Daraio, S. Jin, B. Sadanadan, and A.M. Rao, *Phys. Rev. B* 69, 153414 (2004)

[75] H.C. Choi, J. Park, and B. Kim, *J. Phys. Chem. B* 109, 4333 (2005)

[76] R. Czerw, M. Terrones, J.-C. Charlier, X. Blase, B. Foley et al., *Nano Lett.* 1, 457 (2001)

[77] G. Ertl, J. Küppers, "*Low energy electrons and surface chemistry*", VCH (1985)

[78] P.M. Ajayan, S. Iijima, and T. Ichihashi, *Phys. Rev. B* 47, 6859 (1993)

[79] B.W. Reed and M. Sarikaya, *Phys. Rev. B* 64, 195404 (2001)

[80] T. Pichler, M. Knupfer, M.S. Golden, J. Fink, A. Rinzler and R.E. Smalley, *Phys. Rev. Lett.* 80, 4729 (1998)

[81] M. De Crescenzi, "*Electron Scattering and Related Spectroscopies*", World Scientific Publishing (1996)

[82] H. Lüth, "*Surfaces and interfaces of solid materials*", Springer (1996)

[83] G. Chiarello, E. Maccallini, R.G. Agostino, V. Formoso, A. Cupolillo et al., *Carbon* 41, 985 (2003)

[84] J.H. Fink and Ph. Lambin, *Topics in Appl. Phys.* 80, 247 (2001)

[85] H. Ibach and D.L. Mills, "*Electron energy loss spectroscopy and surface vibrations*", Academic press (1982)

[86] G. Chiarello, E. Maccallini, R.G. Agostino, T. Caruso, V. Formoso et al., *Phys. Rev. B* 69, 153409 (2004)

[87] S. Hüfner, "*Photoelectron Spectroscopy*", Springer (2003)

[88] A. Goldoni, R. Larciprete, L. Gregoratti, B. Kaulich, M. Kiskinova et al., *Appl. Phys. Lett.* 80, 2165 (2005)

[89] N. Bendiab, E. Anglaret, J.-L. Bantignies, A. Zahab, J. L. Sauvajol et al., *Phys. Rev. B* 64, 245424 (2001)

[90] A. Claye, S. Rahman, J.E. Fischer, A. Sirenko, G.U. Sumanasekera, and P.C. Eklund, *Chem. Phys. Lett.* 333, 16 (2001)

[91] E. Jouguelet, C. Mathis and P. Petit, *Chem. Phys. Lett.* 318, 561 (2000)

[92] C. Jo, C. Kim and Y. H. Lee, *Phys. Rev. B* 65, 035420 (2002)

[93] J.E. Demuth, B.N.J. Persson, and A.J. Schell-Sorokin, *Phys. Rev. Lett.* 51, 2214 (1983)

[94] B.N.J. Persson, J.E. Demuth, *Phys. Rev. B* 30, 5968 (1984)

[95] M.K. Kelly, E. Colavita, G. Margaritondo, J. Anderson, L. Papagno, et al., *Phys. Rev. B* 32, 2693 (1985)

[96] J.E. Demuth and B.N.J. Persson, *Phys. Rev. Lett.* 54, 584 (1985)

[97] G.D. Mahan, *Phys. Rev.* 163, 612 (1967)

[98] L. Petaccia, A. Goldoni, S. Lizzit, and R. Larciprete, *J. Electron Spectrosc. Relat. Phenom.* 144, 793 (2005)

[99] S.L. Qiu, C.L. Lin, J. Chen, and M. Strongin, *Phys. Rev. B* 39, 6194 (1989)

[100] G. Zhuang, Y. Chen, and P.N. Ross Jr., *Surf. Sci.* 418, 139 (1998)

[101] A. Cupolillo, C. Giallombardo and L. Papagno, submitted to *Surf. Sci.*

[102] A. Sindona, A. Cupolillo, F. Plastina, C. Giallombardo, G. Falcone, and L. Papagno, *Surf. Sci.*, in press

[103] Q. Zhao, M.B. Nardelli, and J. Bernholc, *Phys. Rev. B* 65, 144105 (2002)

[104] I. Shimoyama, G. Wu, T. Sekiguchi, and Y. Baba, *Phys. Rev. B* 62, R6053 (2000)

[105] M. Mehring, W. Scherer, and A. Weidinger, *Phys. Rev. Lett* 93, 206603 (2004)

[106] J. Hu, P. Yang, and C.M. Lieber, *Phys. Rev. B* 57, R3185 (1998)

[107] S. Souto, M. Pickholz, M.C. dos Santos, and F. Alvarez, *Phys. Rev. B* 57, 2536 (1998)

[108] F. Xu, M. Minniti, C. Giallombardo, A. Cupolillo, P. Barone, A. Oliva, and L. Papagno, submitted to *Surf. Sci.*

[109] P.M. Ajayan and T.W. Ebbesen, *Rep. Prog. Phys.* 60, 1025 (1997)

[110] T.W. Ebbesen and P.M. Ajayan, *Nature* 358, 220 (1992)

[111] K. Anazawa, K. Shimotani, C. Manabe, H. Watanabe, and M. Shimizu, *Appl. Phys. Lett.* 81, 739 (2002)

[112] S.J. Lee, H.K. Baik, J.-e. Yoo, and J.H. Han, *Diamond Relat. Mater.* 11, 914 (2002)

[113] D.S. Bethune, C.H. Kiang, M.S. de Vires, G. Gorman, R. Savoy et al., *Nature* 363, 605 (1993)

[114] T. Guo, P. Nikolaev, A. Thess, D.T. Colbert, and R.E. Smalley, *Chem. Phys. Lett.* 243, 49 (1995)

[115] A. Thess, R. Lee, P. Nikolaev, H. Dai, P. Petit et al., *Science* 273, 483 (1996)

[116] H. Dai, *Surf. Sci.* 500, 218 (2002)

[117] M.S. Dresselhaus, G. Dresselhaus, A. Jorio, A.G. Souza Filho, and R. Saito, *Carbon* 40, 2043 (2002)

[118] Y. Ando, X. Zhao, H. Kataura, Y. Achiba, K. Kaneto et al., *Diamond Relat. Mater.* 9, 847 (2000)

[119] M. Jinno, S. Bandow, and Y. Ando, *Chem. Phys. Lett.* 398, 256 (2004)

[120] Z.Wang, X. Ke, Z. Zhu, F. Zhang, M. Ruan and J. Yang, *Phys. Rev. B* 61, 2472 (2000)

[121] Á. Rusznyák, V. Zólyomi, J. Kürti, S. Yang, M. Kertesz, *Phys. Rev. B* 72, 155420-1-6 (2005)

[122] L. Ravagnan, F. Siviero, C. Lenardi, P. Piseri, E. Barborini et al., *Phys. Rev. Lett.* 89, 285506-1-4 (2002)

[123] C.S. Casari, A. Li Bassi, L. Ravagnan, F. Siviero, C. Lenardi, et al., *Carbon* 42**,** 1103 (2004)

[124] Y. Liu, R.O. Jones, X. Zhao and Y. Ando, *Phys. Rev. B* 68, 125413-1-7 (2003)

[125] J.W. Chen, L.F. Yang, H.T. Yang, J.M. Dong, *Phys. Lett. A* 316, 101 (2003)

[126] M. Jinno, Y.Ando, S.Bandow, J.Fan, M. Yudasaka, and S. Iijima, *Chem. Phys. Lett.* 418, 109 (2006)

[127] E. Cazzanelli, L. Caputi, M. Castriota, A. Cupolillo, C. Giallombardo, and L. Papagno, submitted to *Surf. Sci.*

[128] E. Cazzanelli, M. Castriota, L. Caputi, A. Cupolillo, C. Giallombardo, and L. Papagno, submitted to *Phys. Rev. Lett.*